

REPORT DOCUMENTATION PAGE			Form Approved OMB NO. 0704-0188		
<p>The public reporting burden for this collection of information is estimated to average 1 hour per response, including the time for reviewing instructions, searching existing data sources, gathering and maintaining the data needed, and completing and reviewing the collection of information. Send comments regarding this burden estimate or any other aspect of this collection of information, including suggestions for reducing this burden, to Washington Headquarters Services, Directorate for Information Operations and Reports, 1215 Jefferson Davis Highway, Suite 1204, Arlington VA, 22202-4302. Respondents should be aware that notwithstanding any other provision of law, no person shall be subject to any penalty for failing to comply with a collection of information if it does not display a currently valid OMB control number.</p> <p>PLEASE DO NOT RETURN YOUR FORM TO THE ABOVE ADDRESS.</p>					
1. REPORT DATE (DD-MM-YYYY) 02-05-2011		2. REPORT TYPE Final Report		3. DATES COVERED (From - To) 1-May-2006 - 30-Apr-2011	
4. TITLE AND SUBTITLE Abiotic Supramolecular Systems			5a. CONTRACT NUMBER W911NF-06-1-0116		
			5b. GRANT NUMBER		
			5c. PROGRAM ELEMENT NUMBER 106013		
6. AUTHORS Chad A. Mirkin, Joseph T. Hupp			5d. PROJECT NUMBER		
			5e. TASK NUMBER		
			5f. WORK UNIT NUMBER		
7. PERFORMING ORGANIZATION NAMES AND ADDRESSES Northwestern University Chicago Campus Office of Sponsored Research Northwestern University Evanston, IL 60208 -1110			8. PERFORMING ORGANIZATION REPORT NUMBER		
9. SPONSORING/MONITORING AGENCY NAME(S) AND ADDRESS(ES) U.S. Army Research Office P.O. Box 12211 Research Triangle Park, NC 27709-2211			10. SPONSOR/MONITOR'S ACRONYM(S) ARO		
			11. SPONSOR/MONITOR'S REPORT NUMBER(S) 49632-CH.2		
12. DISTRIBUTION AVAILABILITY STATEMENT Approved for Public Release; Distribution Unlimited					
13. SUPPLEMENTARY NOTES The views, opinions and/or findings contained in this report are those of the author(s) and should not be construed as an official Department of the Army position, policy or decision, unless so designated by other documentation.					
14. ABSTRACT The goal of this research project was to develop new concepts for the preparation of supramolecular and larger structures with unusual and desirable properties based upon coordination chemistry. The following objectives were specifically targeted: (1) new and flexible types of supramolecular allosteric catalysts, (2) MOFs capable of recognizing and separating molecules in novel and efficient ways, (3) bio-inspired structures that facilitate directional energy transfer, and (4) a new class of selective and extremely sensitive chemical sensors based on					
15. SUBJECT TERMS					
16. SECURITY CLASSIFICATION OF:			17. LIMITATION OF ABSTRACT UU	15. NUMBER OF PAGES	19a. NAME OF RESPONSIBLE PERSON Chad Mirkin
a. REPORT UU	b. ABSTRACT UU	c. THIS PAGE UU			19b. TELEPHONE NUMBER 847-467-7302

Report Title

Abiotic Supramolecular Systems

ABSTRACT

The goal of this research project was to develop new concepts for the preparation of supramolecular and larger structures with unusual and desirable properties based upon coordination chemistry. The following objectives were specifically targeted: (1) new and flexible types of supramolecular allosteric catalysts, (2) MOFs capable of recognizing and separating molecules in novel and efficient ways, (3) bio-inspired structures that facilitate directional energy transfer, and (4) a new class of selective and extremely sensitive chemical sensors based on signal transduction and signal amplification strategies within supramolecular assemblies. The progress made over the grant period is detailed in this report.

List of papers submitted or published that acknowledge ARO support during this reporting period. List the papers, including journal references, in the following categories:

(a) Papers published in peer-reviewed journals (N/A for none)

1. "Chemical reduction of a diimide based porous polymer for selective uptake of carbon dioxide versus methane," O. K. Farha, Y. Bae, B. G. Hauser, A. M. Spokoyny, R. Q. Snurr, C. A. Mirkin and J. T. Hupp, Chem. Commun., 2010, 46, 1056-1058.
2. "Porosity Tuning of Carborane-Based Metal Organic Frameworks (MOFs) via Coordination Chemistry and Ligand Design," A.M. Spokoyny, O.K. Farha, K. L. Mulfort, J. T. Hupp, and C. A. Mirkin, Inorg. Chim. Acta, 364, 2010, 266-271 (Arnold Rheingold commemorative issue).
3. "A 'click-based' porous organic polymer from tetrahedral building blocks," J. T. Hupp, et al., J. Mater. Chem., 21, 2011, 1700-1703.
4. "SiO₂ Aerogel-Templated, Porous TiO₂ Photoanodes for Enhanced Performance in Dye-Sensitized Solar Cells Containing a Ni(III)/(IV) Bis(dicarbollide) Shuttle," T. C. Li, F. Fabregat-Santiago, O. K. Farha, A. M. Spokoyny, S. Ruiz, J. Bisquert, C. A. Mirkin, T. J. Marks, and J. T. Hupp, J. Phys. Chem. C, 2011, accepted.
5. "The Plasticity of the Nickel(II) Coordination Environment in Complexes with Hemilabile Phosphino-Thioether Ligands," Machan, C. W.; Spokoyny, A. M.; Jones, M. R.; Sarjeant, A. A.; Stern, C. L.; Mirkin, C. A. J. Am. Chem. Soc., 2011, 133(9), 3023-33.
6. "Allosteric Supramolecular Triple-Layer Catalysts," Yoon, H. J.; Kuwabara, J.; Kim, J.-H.; Mirkin, C. A. Science, 2010, 330, 66-69.

Number of Papers published in peer-reviewed journals: 6.00

(b) Papers published in non-peer-reviewed journals or in conference proceedings (N/A for none)

Number of Papers published in non peer-reviewed journals: 0.00

(c) Presentations

1. Seminar speaker, Dept. of Chemistry, Loyola University, March, 2010. (Hupp)
2. Seminar speaker, Dept. of Chemistry, University of Texas, March, 2010. (Hupp)
3. Distinguished Alumni Lecture, Dept. of Chemistry, Michigan State University, April, 2010. (Hupp)
4. Gordon Research Conference on Solid State Chemistry, New Hampshire, July, 2010. (Hupp)
5. CB DTRA Program Review Conference, Virginia, August, 2010. (Hupp)
6. Symposium on Solar Energy Conversion, ACS National Meeting, Boston, August, 2010. (Hupp)
7. Symposium on Fuels, ACS National Meeting, Boston, August, 2010. (Hupp)
8. DTRA Chem/Bio Filtration Strategies Working Group, September, 2010. HUPP
9. Seminar speaker, Dept. of Chemistry, University of Wisconsin, October, 2010. (Hupp)
10. Distinguished Lecturer Series, Energy Research Center, University of Notre Dame, November, 2010. (Hupp)
11. Symposium on Functional Metal-Organic Framework Materials, Pacificchem, Honolulu, December, 2010. (Hupp)
12. Symposium on Catalytic Metal-Organic Framework Materials, Pacificchem, Honolulu, December, 2010. (Hupp)
13. AFOSR-MURI Program Review, Maryland, January, 2010. (Hupp)
14. Seminar speaker, Dept. of Chemistry, University of Pennsylvania, February, 2011. (Hupp)
15. Seminar speaker, Dept. of Chemistry, MIT, February, 2011. (Hupp)
16. Kolthoff Lecturer, University of Minnesota, February, 2011. (Hupp)
17. Feinberg School of Medicine's Distinguished Lecture in Life Sciences, Northwestern University, Chicago, IL; "The Polyvalent Gold Nanoparticle Conjugate: A New Paradigm in Molecular Diagnostics and Intracellular Gene Regulation," 2010, (Mirkin)
18. Institute of Electrical and Electronics Engineers conference, Plenary Speaker, Seoul, Korea; "Molecular Printing: A Chemist's Approach to a Desktop Fab," 2010, (Mirkin)
19. University of Calgary, Distinguished Visiting Speaker, Calgary, Alberta, Canada; "The Polyvalent Gold Nanoparticle Conjugate: Materials Synthesis, Biodiagnostics, and Intracellular Gene Regulation," 2010, (Mirkin)
20. Graduate Programs Distinguished Lecturer, Scripps Research Institute, La Jolla, CA; "Polyvalent DNA: A New Frontier in Molecular Diagnostics and Intracellular Gene Regulation," 2010, (Mirkin)
21. Nelson W. Taylor Award Lecture, Pennsylvania State University, University Park, PA; "Molecular Printing: A Chemist's Approach to Desk Top Fab," 2010, (MIRKIN)
22. Keck Seminar, Gordon Research Conference, Houston, TX; "Polyvalent DNA Nanostructures: A New Frontier in Materials Synthesis, Biodiagnostics, and Intracellular Gene Regulation," 2010, Mirkin
23. Einstein Award Lecture, Chinese Academy of Sciences, Beijing, China, "Polyvalent Oligonucleotide Nanoparticle Conjugate: A New Frontier in Materials Synthesis, In Vitro Diagnostics, and Intracellular Gene Regulation," 2010, (Mirkin)
24. Distinguished Truman Lecture, Sandia National Laboratories, Albuquerque, NM; "Molecular Printing: A Chemist's Approach a Desk Top Fab," 2011 (Mirkin)
25. Plenary Talk, Lab Automation conference, Palm Springs, CA; "The Polyvalent Oligonucleotide Nanoparticle Conjugate: A New Frontier in In Vitro Diagnostics and Intracellular Gene Regulation," 2011, (Mirkin)
26. Plenary Talk, Pittcon Annual Conference, Atlanta, GA; "Polyvalent DNA Architecture: New Modalities for Intracellular Gene Regulation and Detection," 2011, (Mirkin)
27. Pacificchem, Honolulu, HI, "Nanostructure Synthesis with Plasmonic Seeds", "Coordination-Based Abiotic Molecular Machines", and "Novel Forms of Biolabeling and Amplification Afforded by Structures Generated by On-Wire Lithograph," 2010, (Mirkin)

Number of Presentations: 27.00

Non Peer-Reviewed Conference Proceeding publications (other than abstracts):

Number of Non Peer-Reviewed Conference Proceeding publications (other than abstracts): 0

Peer-Reviewed Conference Proceeding publications (other than abstracts):

Number of Peer-Reviewed Conference Proceeding publications (other than abstracts): 0

(d) Manuscripts

Number of Manuscripts: 0.00

Patents Submitted

Patents Awarded

Awards

Hupp, Joseph T., Co-chair, 2011 Gordon Research Conference on “Renewable Energy: Solar Fuels”.

Hupp, Joseph T., Program Review Committee for Nanoscience Center at Northern Illinois University (2011)

Hupp, Joseph T., Houghton College Alumnus of the Year, 2010.

Hupp, Joseph T., Distinguished Alumni Lecturer, Michigan State University, 2010.

Mirkin, Chad A., Elected Member of the Institute of Medicine, 2010.

Mirkin, Chad A., Thomson Reuters Most Cited Chemist in the World (#1, based on total citations), 2010.

Mirkin, Chad A., Nelson W. Taylor Award, Department of Materials Science and Engineering, Penn State, 2010.

Mirkin, Chad A., Elected Member of the National Academy of Sciences, 2010.

Mirkin, Chad A., Herman S. Bloch Award for Scientific Excellence in Industry, University of Chicago, 2010.

Mirkin, Chad A., Einstein Professorship of the Chinese Academy of Sciences (CAS), 2010.

Mirkin, Chad A., Ohio State University Edward Mack Jr. Memorial Award, 2010.

Graduate Students

<u>NAME</u>	<u>PERCENT SUPPORTED</u>
Charles William Machan	1.00
Aleksandr Spokognyy	1.00
FTE Equivalent:	2.00
Total Number:	2

Names of Post Doctorates

<u>NAME</u>	<u>PERCENT SUPPORTED</u>
Omar Farha	0.28
Chang Yeon Lee	0.35
Ho-Jin Son	0.30
FTE Equivalent:	0.93
Total Number:	3

Names of Faculty Supported

<u>NAME</u>	<u>PERCENT SUPPORTED</u>	National Academy Member
Chad A. Mirkin	0.00	Yes
FTE Equivalent:	0.00	
Total Number:	1	

Names of Under Graduate students supported

<u>NAME</u>	<u>PERCENT SUPPORTED</u>
FTE Equivalent:	
Total Number:	

Student Metrics

This section only applies to graduating undergraduates supported by this agreement in this reporting period

The number of undergraduates funded by this agreement who graduated during this period: 0.00

The number of undergraduates funded by this agreement who graduated during this period with a degree in science, mathematics, engineering, or technology fields:..... 0.00

The number of undergraduates funded by your agreement who graduated during this period and will continue to pursue a graduate or Ph.D. degree in science, mathematics, engineering, or technology fields:..... 0.00

Number of graduating undergraduates who achieved a 3.5 GPA to 4.0 (4.0 max scale):..... 0.00

Number of graduating undergraduates funded by a DoD funded Center of Excellence grant for Education, Research and Engineering:..... 0.00

The number of undergraduates funded by your agreement who graduated during this period and intend to work for the Department of Defense 0.00

The number of undergraduates funded by your agreement who graduated during this period and will receive scholarships or fellowships for further studies in science, mathematics, engineering or technology fields: 0.00

Names of Personnel receiving masters degrees

NAME

Total Number:

Names of personnel receiving PHDs

NAME

Hyo Jae Yoon
Michael Wiester

Total Number: 2

Names of other research staff

NAME

PERCENT SUPPORTED

FTE Equivalent:

Total Number:

Sub Contractors (DD882)

Inventions (DD882)

5 Amorphous Infinite Coordination Polymer Microparticles: A New Class of Selective Hydrogen Storage Materials

Patent Filed in US? (5d-1) Y

Patent Filed in Foreign Countries? (5d-2) N

Was the assignment forwarded to the contracting officer? (5e) N

Foreign Countries of application (5g-2):

5a: You-Moon Jeon

5f-1a: Northwestern University

5f-c: 633 Clark Street

Evanston IL 60208

5a: Jungseok Heo

5f-1a: Northwestern University

5f-c: 633 Clark Street

Evanston IL 60208

5a: Chad A. Mirkin

5f-1a: Northwestern University

5f-c: 633 Clark Street

Evanston IL 60208

5 Ni(III)/(IV) Bisdicarbollide as a Fast and Non-Corrosive Redox Shuttle for Dye-Sensitized Solar Cells

Patent Filed in US? (5d-1) N

Patent Filed in Foreign Countries? (5d-2) N

Was the assignment forwarded to the contracting officer? (5e) N

Foreign Countries of application (5g-2):

5a: Chad A. Mirkin

5f-1a: Northwestern University

5f-c: 633 Clark Street

Evanston IL 60208

5a: Alexander M. Spokoyny

5f-1a: Northwestern University

5f-c: 633 Clark Street

Evanston IL 60208

5a: Tina C. Li

5f-1a: Northwestern University

5f-c: 633 Clark Street

Evanston IL 60208

5a: Omar K. Farha

5f-1a: Northwestern University

5f-c: 633 Clark Street

Evanston IL 60208

5a: Joseph T. Hupp

5f-1a: Northwestern University

5f-c: 633 Clark Street

Evanston IL 60208

5 PCR-Like Cascade Reactions in the Context of an Allosteric Enzyme Mimic

Patent Filed in US? (5d-1) Y

Patent Filed in Foreign Countries? (5d-2) N

Was the assignment forwarded to the contracting officer? (5e) N

Foreign Countries of application (5g-2):

5a: Chad A. Mirkin

5f-1a: Northwestern University

5f-c: 633 Clark Street

Evanston IL 60208

5a: Hyo Jae Yoon

5f-1a: Northwestern University

5f-c: 633 Clark Street

Evanston IL 60208

5 Pincer Complexes Constructed From Boron-Rich Clusters

Patent Filed in US? (5d-1) Y

Patent Filed in Foreign Countries? (5d-2) N

Was the assignment forwarded to the contracting officer? (5e) N

Foreign Countries of application (5g-2):

5a: Alex Spokoyny

5f-1a: Northwestern University

5f-c: 633 Clark Street

Evanston IL 60208

5a: Chad A. Mirkin

5f-1a: Northwestern University

5f-c: 633 Clark Street

Evanston IL 60208

Scientific Progress

Technology Transfer

ABIOTIC SUPRAMOLECULAR SYSTEMS

Final Report April 30th, 2011

Sponsor Award Number: W911NF-06-1-0116

PI: Chad A. Mirkin, Northwestern University

Statement of Work

The goal of this research was to develop new concepts for the preparation of supramolecular and larger structures with unusual and desirable properties based upon coordination chemistry. The following objectives were specifically targeted: (1) new and flexible types of supramolecular allosteric catalysts, (2) MOFs capable of recognizing and separating molecules in novel and efficient ways, (3) bio-inspired structures that facilitate directional energy transfer, and (4) a new class of selective and extremely sensitive chemical sensors based on signal transduction and signal amplification strategies within supramolecular assemblies.

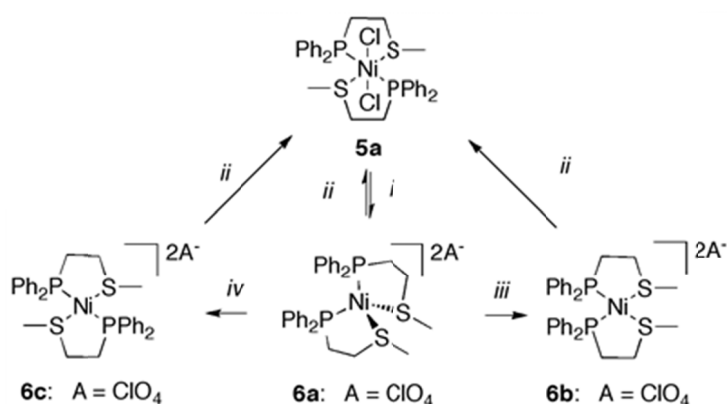
Objectives 1 and 4: New and flexible types of supramolecular allosteric catalysts and a new class of selective and extremely sensitive chemical sensors based on signal transduction and signal amplification strategies within supramolecular assemblies.

1. Allosterically Regulated Geometric Transformations in Ni(II) Complexes.

Several coordination chemistry-based methods for preparing supramolecular macrocycles and cage structures have been developed, one of these being the weak-link approach (WLA) which can be used to synthesize inorganic complexes of various and complex geometries from readily available hemilabile ligands and metal precursors. Importantly, the species formed from the WLA can be interconverted between rigid and flexible structures through small molecule reactions at the metal sites, thus providing a powerful platform for constructing abiotic allosteric

enzyme mimics. The approach is extremely general and has been applied to many different metal centers, which has dramatically increased the scope of its utility in catalysis and biomimetic systems. The ability to form closed complexes with a variety of metal centers (mostly d⁸) and appropriate hemilabile ligands has created a library of chemical reactions that involve the use of small molecules or elemental anions to control the in situ closing and opening of such complexes, often into catalytically active forms. Interestingly, Ni(II) has been conspicuously absent from the

Scheme 1. Reaction scheme for formation of **6a-c**.^a

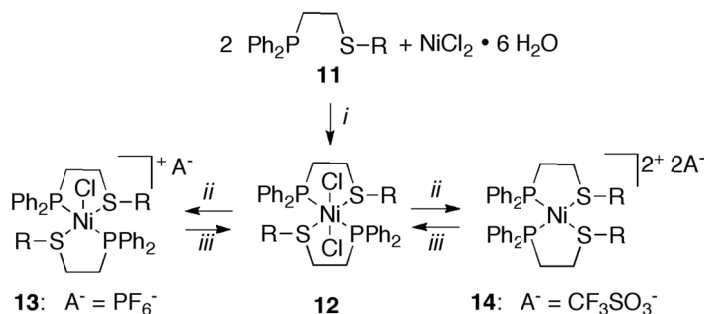


^a (i) 2 eq. LiClO₄/CH₂Cl₂, 1 hr; (ii) = 2 eq. Bis(triphenylphosphine)iminium chloride/CH₂Cl₂; (iii) = solvent layering Et₂O/CH₂Cl₂; (iv) = **6c**: excess LiClO₄/CH₂Cl₂, 3 days.

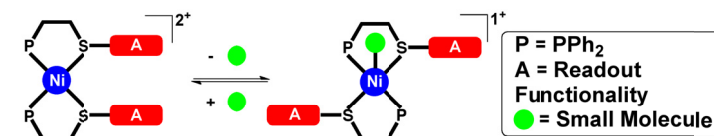
list of metal centers that has been explored with respect to the WLA, and therefore, we decided to investigate the potential of using it to form homoligated structures from phosphinoethylthioether hemilabile ligands. Based on the previously reported understanding of the solution behavior of **5a** (Scheme 1), we decided to probe the generality of this behavior with respect to functionalized phosphinoalkyl thioether ligands. To accomplish this we synthesized a series of model complexes (**12-14**, Scheme 2) with the ultimate goal of creating a detection scheme for a variety of analyte molecules, by triggering a geometric change at the Ni(II) center (Scheme 3).

Similar to the synthesis of **5a**, by reacting two equivalents of a (2-(2-naphthalene)-thioethyl)diphenylphosphine ligand, **11**, with $\text{Ni}[\text{ClO}_4]_2 \cdot 6 \text{H}_2\text{O}$, we prepared and were able subsequently to isolate a new complex, **12** (Scheme 2). The solid-state structure of **12** was determined by a single-crystal X-ray diffraction study carried out with crystals grown by layering Et_2O on top of a CH_2Cl_2 solution of this material. In the solid state, complex **12** has an octahedral geometry similar to that observed for **5a** (Figure 1A), and its fluxional behavior as observed by $^{31}\text{P}\{^1\text{H}\}$ NMR spectroscopy shows remarkable similarities as well. All other characterization data are consistent with the proposed structural formulation of **12**.

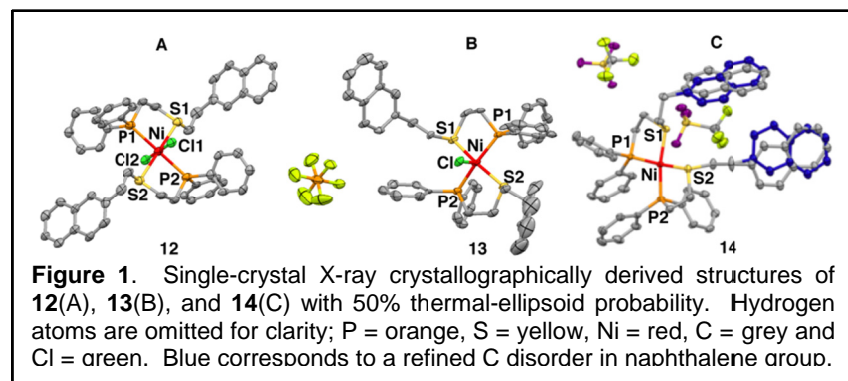
Scheme 2. Reaction scheme for the formation of **12**, **13**, and **14** where R = (2-naphthalene)-ethyl.^a



^a (i) EtOH , 1 hr; (ii) 2 eq. $\text{Tl}(\text{CF}_3\text{SO}_3)$ (**14**) or 1 eq. TIPF_6 (**13**) in CH_2Cl_2 ; (iii) 1 or 2 eq. $\text{PPN}^+\text{Cl}^-/\text{CH}_2\text{Cl}_2$.



Scheme 3. Proposed reaction pathway for analyte detection via Ni(II) WLA.



for an X-ray diffraction study were grown by layering Et_2O on top of a CH_2Cl_2 solution of **13**. A single-crystal X-ray diffraction study shows that **13** (Figure 1B) is a square-pyramidal complex with two fully chelated equivalents of phosphinoalkylthioether ligand **11** around the Ni center in a *trans* arrangement with a single apical Cl^- ligand. The X-ray crystal structure of **13** exhibits a Ni–Cl bond longer (2.456(3) Å) than the Ni–Cl bonds in **12** (2.3635(17) Å). This Ni–Cl bond

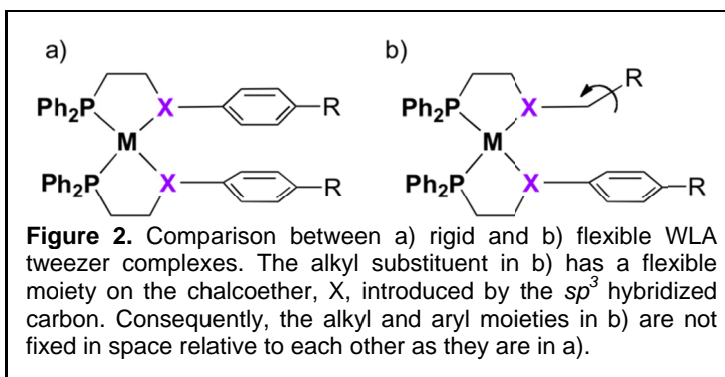
Interestingly, the mono- Cl^- adduct complex **13** can be synthesized from **12** by the addition of one equivalent of TIPF_6 in CH_2Cl_2 . This red compound, when dissolved in CD_2Cl_2 , showed a single resonance in its $^{31}\text{P}\{^1\text{H}\}$ NMR spectrum at δ 51. Single crystals of **13** suitable

length is the longest observed for all crystallographically characterized Ni(II) complexes discussed in this manuscript. Interestingly, in **13** the two Ni–S bond lengths are almost identical to the two Ni–P bond lengths.

It was also possible to isolate an analogue of **6b** for complex **12** under complete chloride-abstracting conditions. The addition of two equivalents of thallium(I) triflate (TlCF₃SO₃) to a solution of **12** in CH₂Cl₂ yielded a deep red solution, which when filtered and reduced to dryness under vacuum, gave a red powder, **14**. When this powder was dissolved in CD₂Cl₂ and characterized by ³¹P{¹H} NMR spectroscopy, it showed a single resonance at δ 58. Layering Et₂O on top of a solution of **14** in CH₂Cl₂ yielded single crystals suitable for an X-ray diffraction study. This structural study showed a square-planar complex with a *cis* arrangement of two equivalents of **11** around the Ni center, similar to that observed in the complexes determined when **5a** was reacted with chloride abstracting agents. The crystal structure of **14** exhibited Ni–P and Ni–S bond lengths, which were very similar to the isoelectronic analogue **6b**. As mentioned above, the conformational flexibility of the ethyl spacer and asymmetric attachment of the naphthalene to the S moiety on ligand **11** allows for multiple orientations, which creates disorder in the solid-state. Indeed, two dominant conformations were resolved in the refined crystal structure of **14** (the secondary positions for the naphthalene groups are shown in blue in **Figure 1C**). These initial results lead us to believe that it will indeed be possible to synthesize a Ni(II) centered detection scheme, wherein the alignment of moieties appended to ligands can be reversibly controlled in solution by reactions at the metal center.

2. Development of Robust and Air-Stable WLA Systems via Pt(II) Coordination Chemistry.

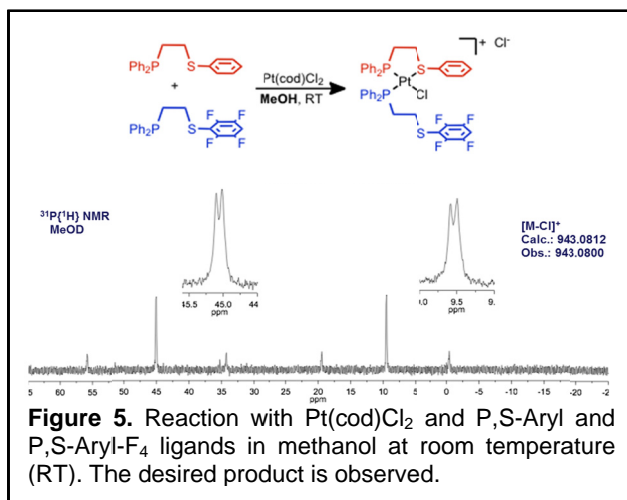
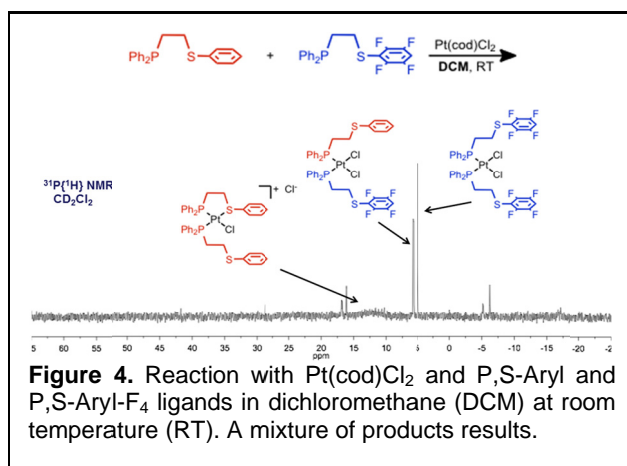
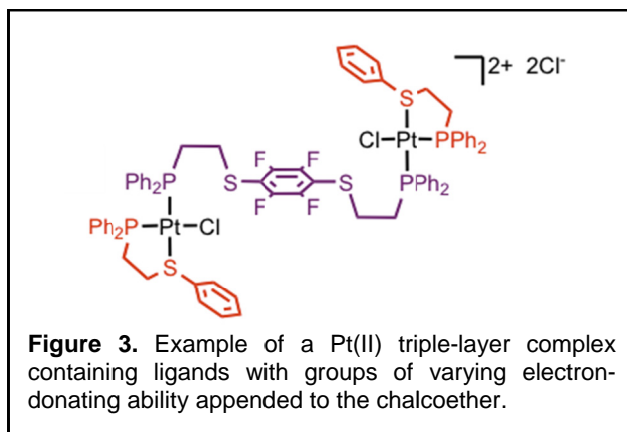
The Weak-Link Approach (WLA) was used to synthesize a class of multimetallic allosteric complexes whose molecular recognition and catalytic abilities have been studied extensively. The majority of the catalysts synthesized *via* the WLA were based on homoligated macrocycles or tweezers and only supported the use of bimetallic catalysts. Recently, we reported the synthesis of a triple-layer complex (TLC), comprising two Rh(I) nodes and two chemically inert blocking layers shielding a catalytically-active inert inner layer. Significantly, this motif allows for the use of monometallic catalysts, opening a myriad of possibilities in the area of allosteric catalysis. However, the utility of TLC-based allosteric catalysts is limited by 1) the use of Rh(I), which makes air-sensitive complexes and 2) the lack of rigidity introduced by the methyl group appended to the chalcogen in Pt(II) model complexes (**Figure 2**). While model Pt(II) macrocycle and tweezer complexes containing only aryl substituents on the chalcogen (for rigidity) have been synthesized, Pt(II)-containing TLC compounds with only aryl substituents have thus far been elusive. While the diphenylphosphine interacts strongly with the Pt(II) center, it is not coordinated to the metal all the time. In order to obtain supramolecular systems whose robustness rivals, and even exceeds, that of enzymes, a stronger ligand-metal interaction is needed. Consequently, the goals of this research were to synthesize Pt(II)-based TLC architectures not reliant on

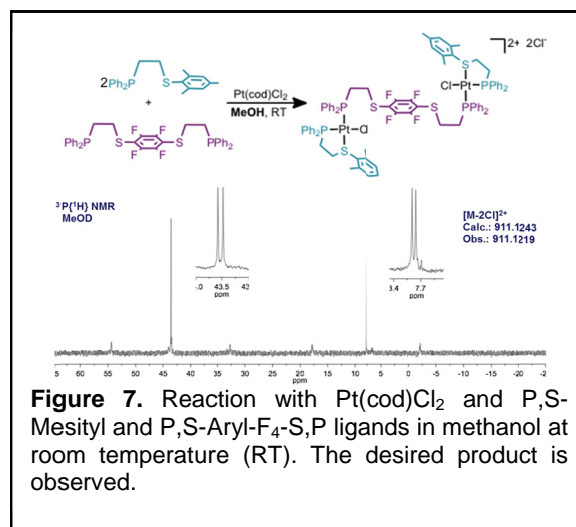
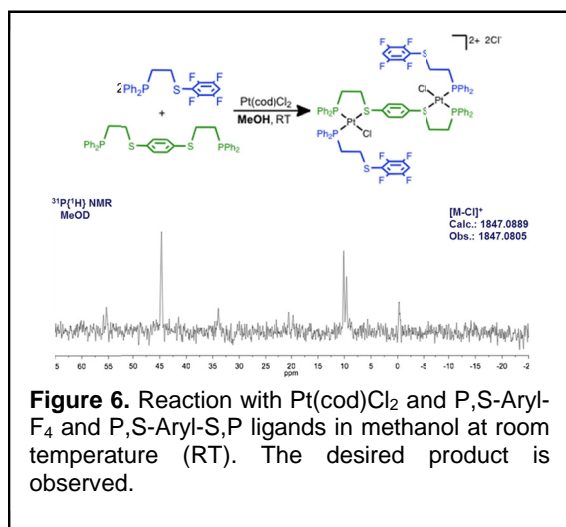


P-based ligands.

Recently we have learned from fundamental studies on model Pt(II) tweezer complexes that heteroligated complex formation with Pt(II) can only be obtained when the ligands in the WLA complex had moieties with differing electron-donating abilities appended to the chalcogenethers. Consequently, we targeted complexes such as the one shown in **Figure 3**, where the electron-donating ability of the substituents on the chalcogenether is varied through the use of phenyl and tetrafluorophenyl moieties. However, during a study using a model tweezer complex and P,S-Aryl and P,S-Aryl-F₄ ligands, we found that the traditional synthesis of these complexes in dichloromethane (DCM) was not successful, as a mixture of products resulted (**Figure 4**). However, further study indicated that using methanol as a solvent resulted in *in situ* quantitative yield of the desired tweezer complex (**Figure 5**). Consequently, this synthetic technique was used to synthesize the model TLC complex shown in **Figure 3** as well as the variations shown in **Figures 6** and **7**. Heteronuclear NMR spectroscopy (³¹P{¹H}) and High-Resolution Electrospray Ionization Mass Spectroscopy have been thus far used to characterize these complexes.

The next step is to abstract all of the chloride ligands from the complexes, making them fully-closed, such that the model blocking ligands shield the middle layer of the complex. However, the typical abstracting agents used for this purpose cannot be used here: silver salts in methanol form AgOH, which is incompatible with the complexes and sodium salts are not ideal because NaCl is soluble in methanol. Consequently, other solvents, including tetrahydrofuran, nitromethane, and acetonitrile were explored. Unfortunately, the semi-open complex is only stable in methanol. Consequently, other routes to chloride abstraction, including the use of thallium salts are being explored. Once we are able to toggle between the semi-open and closed states, we will synthesize functional Pt(II) TLC complexes for use in sophisticated allosteric catalytic systems.

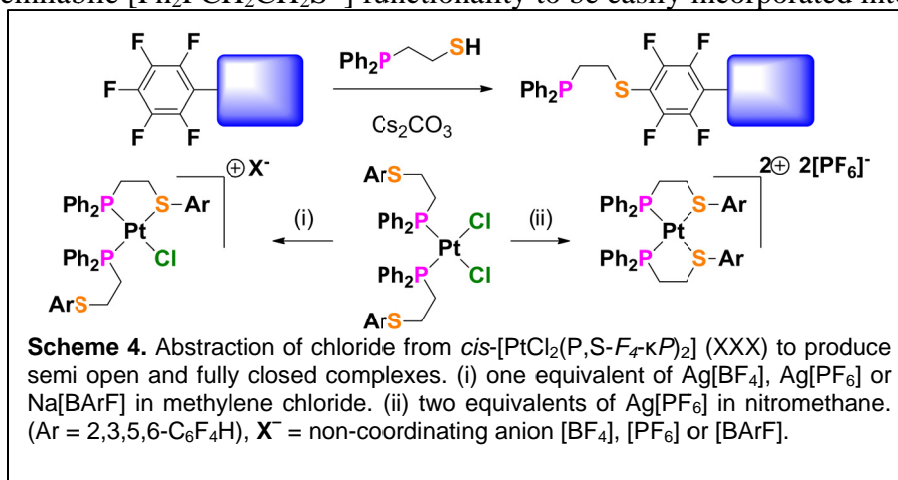




3. Expanding the Analyte Pool: Reactions of Pt(II) Tweezers with Small Molecules.

The chemistry of rhodium(I) complexes which possess hemilabile phosphinoether and phosphinothioether ligands has been well explored. However, although the system is predictable and well behaved, it has some serious shortcomings. One problem is the sensitivity of the Rh(I) complexes to air, necessitating the chemistry to be conducted in a glove box or using careful Schlenk techniques. This severely limits the potential applications of systems that incorporate Rhodium. Another shortcoming is the small variety of ligands (e.g. chloride, carbon monoxide and acetate) which may bind to the rhodium center in order to break the weak link and induce a change in the geometry of the complex. The analogous Pt(II) complexes, on the other hand, are robust and air-stable and there is a potentially large variety of ligands which can bind to Pt(II) in order to break a weak link. Attractive as platinum may be for the construction of supermolecular complexes using the weak-link approach, the chemistry of Pt(II) complexes with hemilabile ligands is underexplored in comparison to the related chemistry of Rh(I) and requires further investigation if it is to become part of the WLA toolbox.

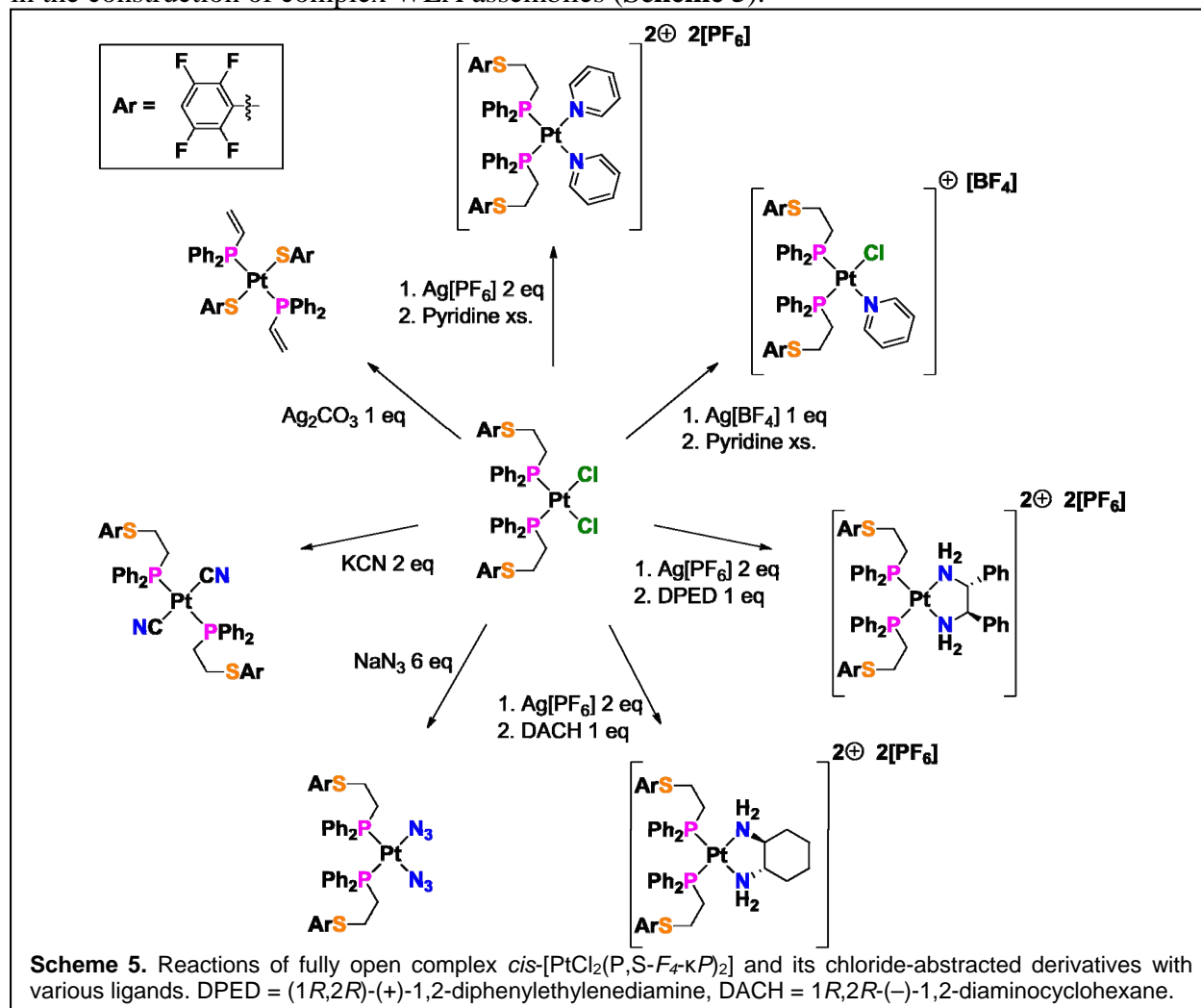
We have found that the nucleophilic aromatic substitution reaction between the cesium salt, $\text{Cs}^+[\text{Ph}_2\text{PCH}_2\text{CH}_2\text{S}^-]$, and a pentafluorophenyl group occurs cleanly and reliably at the *para* position. This allows the hemilabile $[\text{Ph}_2\text{PCH}_2\text{CH}_2\text{S}^-]$ functionality to be easily incorporated into complex molecules. Furthermore, the electron-withdrawing tetrafluorophenylene group reduces the strength of the thioether-metal weak link, which increases the versatility of the ligand. For example, in the case of platinum, closed, semi-open and fully open coordination modes are



accessible simply by introducing or abstracting chloride. In order to investigate the behavior of the such fluorinated systems, the model complex *cis*-[PtCl₂(P,S-*F*₄-κP)₂] (**Scheme 4**), where (P,S-*F*₄) is the hemilabile ligand Ph₂PCH₂CH₂SAr (Ar = 2,3,5,6-C₆F₄H), was studied.

The simple chloride-abstraction chemistry of *cis*-[PtCl₂(P,S-*F*₄-κP)₂] is shown in Scheme 4. Several anionic, neutral and chelating ligands were investigated with this system. Acetonitrile is not a strong enough ligand to displace chloride from *cis*-[PtCl₂(P,S-*F*₄-κP)₂], even in the presence of methanol. Acetonitrile also does not displace the sulfur atoms of the chelating P,S-*F*₄ ligands of the fully closed species, either in solution or in the solid state (single-crystal XRD).

This behavior contrasts with that of hemilabile ligand-containing complexes based on the previously investigated metal elements Rh, Pd and Cu, which readily coordinate acetonitrile with the concomitant severing of the weak link. This suggests that acetonitrile may be a useful solvent for Pt(II) WLA chemistry. Pyridine, on the other hand, displaces chloride, but only in the presence of methanol. Pyridine readily displaces the sulfur atoms of the chelating P,S-*F*₄ ligands of the fully closed complex *cis*-[Pt(P,S-*F*₄-κP,κS)₂][BF₄]₂ in methylene chloride to form the open complex *cis*-[Pt(P,S-*F*₄-κP)₂(NC₅H₅-κN)₂][BF₄]₂, confirmed *via* single-crystal XRD. Thus pyridine is a stronger ligand than acetonitrile, which suggests that pyridyl groups may find utility in the construction of complex WLA assemblies (**Scheme 5**).

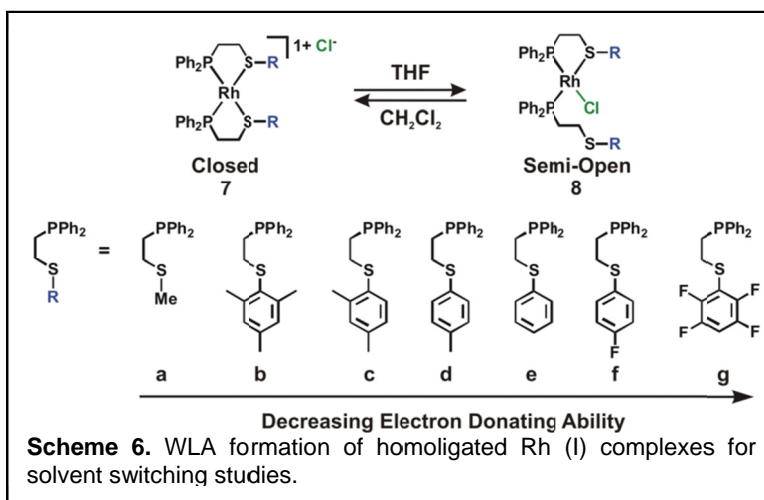


When one equivalent of (1*R*,2*R*)-(+)-1,2-diphenylethylenediamine [(+)-DPED] is added to a solution of *cis*-[PtCl₂(P,*S*-*F*₄-κ*P*)₂] in methylene chloride-*d*₂, no reaction is observed via ³¹P{¹H} NMR spectroscopy. In methanol-*d*₄, however, the clean conversion to the chelated species *cis*-[Pt(P,*S*-*F*₄-κ*P*)₂(NH₂(CHPh)₂NH₂-κ²*N*)]Cl₂ is observed. The analogous complex *cis*-[Pt(P,*S*-*F*₄-κ*P*)₂(NH₂(CHPh)₂NH₂-κ²*N*)](PF₆)₂ (**Scheme 5**) is cleanly produced when one equivalent of (+)-DPED is added to the fully closed species *cis*-[Pt(P,*S*-*F*₄-κ*P*,κ*S*)₂](PF₆)₂ in methylene chloride, confirmed *via* single-crystal XRD. A similarly reaction using 1*R*,2*R*-(-)-1,2-diaminocyclohexane produces the chelated complex *cis*-[Pt(P,*S*-*F*₄-κ*P*)₂(NH₂(C₆H₁₀)NH₂-κ²*N*)](PF₆)₂ (**Scheme 5**), as determined using ³¹P{¹H} NMR spectroscopy. This suggests that the binding strength of chelating diamines is superior to that of pyridine.

A number of anionic ligands have also been investigated. When an excess of sodium azide is added to the fully open complex *cis*-[PtCl₂(P,*S*-*F*₄-κ*P*)₂] (**Scheme 5**) in methanol, the fully-open complex *cis*-[Pt(N₃)₂(P,*S*-*F*₄-κ*P*)₂] is formed via chloride substitution. A similar reaction using strictly two equivalents of potassium cyanide in methanol results in the formation of the biscyano complex *trans*-[Pt(CN)₂(P,*S*-*F*₄-κ*P*)₂], confirmed *via* single-crystal XRD. Importantly, in contrast to the case of azide, excess cyanide strips the phosphine ligands from the metal center, producing K₂[PtCN₄]. Attempts to synthesize the neutral bidentate carbonate complex *cis*-[Pt(CO₂-κ²*O*)(P,*S*-*F*₄-κ*P*)₂] via the abstraction of both chlorides from the fully open precursor *cis*-[PtCl₂(P,*S*-*F*₄-κ*P*)₂] using silver carbonate in methylene chloride failed. Rather, clean conversion to the bis(vinylphosphine) complex *trans*-[Pt(SAr-κ*S*)₂(Ph₂PCH=CH₂-κ*P*)₂] (Ar = 2,3,5,6-C₆F₄H) occurred (single-crystal XRD), presumably because of elimination by carbonate across the ethylene bridges of the chelating ligands. This novel reactivity is being investigated. This work has allowed a hierarchy of ligand strength to be established which will aid us greatly in the design and realization of functional WLA supermolecules based on platinum(II).

4. Solvent and Temperature Induced Switching of Tweezer-Like Rh^I Phosphinoalkyl Thioether (PS) Complexes.

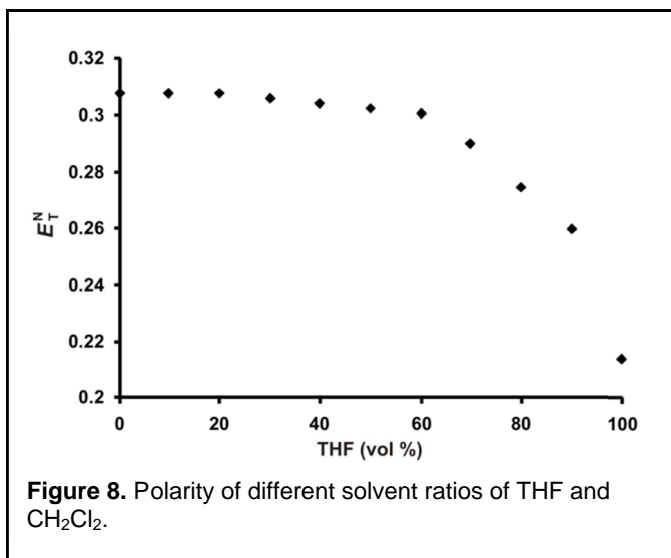
Previously used systems based on the Rh^I metal center used in the WLA did not investigate the importance of solvent choice and its influence on counteranion coordination. This is of vital importance because of the potential impact on catalytic and recognition systems prepared by this method. Because of this importance of the coordination geometry in functional systems prepared via the weak-link approach (WLA), a series of phosphinoalkyl thioether (PS) hemilabile ligands with varying electron donating abilities were synthesized and incorporated into homoligated Rh^I(PS)₂Cl complexes (**Scheme 6**), whose switching between closed and semi-open structural isomers was studied by variable temperature ³¹P NMR spectroscopy in different solvent mixtures of CH₂Cl₂ and THF to obtain thermodynamic parameters (Δ*G*^o, Δ*H*^o, TΔ*S*^o, and *K*_{eq}). These two constitutional isomers differ in the position of the chloride counterion,



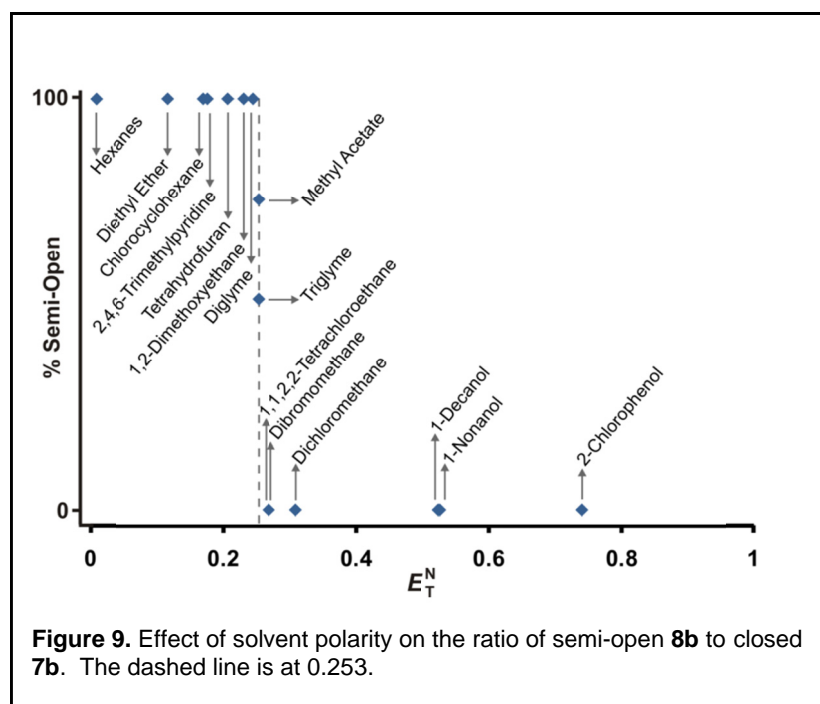
such that the Cl^- anion occupies the outer coordination sphere of the closed isomer, whereas in the semi-open isomer, the Cl^- displaces one of the Rh-S bonds by moving to the inner sphere of the coordination complex. The closed isomer was favored in CH_2Cl_2 and the semi-open isomer favored in THF. The preference for either isomer depends on the solvent polarity, based upon the E_T^N solvent polarity scale, as was determined from 15 different solvents, with more polar solvents favoring the closed isomer. The isomer preference also depends on the electron donating ability of the group attached to the sulfur of the PS ligand, with electron donating groups favoring the closed isomer and electron withdrawing groups favoring the semi-open isomer. The formation of the semi-open isomer from the closed isomer is entropically favored, but enthalpically disfavored. Elucidation of the principles and environments that determine the equilibrium between the two isomers will aid in the design of functional complexes prepared by the WLA.

The switching between inner and outer sphere Cl^- coordination of $\text{Rh}^{\text{I}}(\text{PS})_2\text{Cl}$ complexes **7b-f** and **8b-f** was also studied at different temperatures and solvent mixtures (THF- d_8 : CD_2Cl_2) by VT ^{31}P NMR spectroscopy. It should be noted that no switching was observed for the complexes formed with the most electron donating and most electron withdrawing ligands (**a** and **g**, respectively). For all solvent ratios and temperatures investigated, only the closed isomer **7a** and only the semi-open isomer **8g** were observed by ^{31}P NMR spectroscopy, indicating that strongly electron donating ligands favor the closed isomer, and strongly electron withdrawing ligands favor the semi-open isomer. For the complexes where switching was observed as the solvent ratio and temperature were changed, K_{eq} increases (ΔG° decreases) as the amount of THF- d_8 increases relative to CD_2Cl_2 , signifying that for these complexes the semi-open isomer is also more favored in THF- d_8 .

For complexes **7c-e** and **8c-e**, ΔH° decreases as the amount of THF- d_8 increases, similar to complexes **7b** and **8b**, signifying that there is a lower enthalpy of reaction in less polar solvent mixtures, possibly a result of the solvent not shielding the charges between the Rh^{I} complex and the Cl^- counterion as the values of E_T^N decreases from 0.275 to 0.213 as the solvent mixture increases from 80 to 100% THF- d_8 (**Figure 8**). However, $T\Delta S^\circ$ does not vary significantly as the concentration of THF- d_8 increases, suggesting that the reaction is always entropically favored, regardless of solvent polarity. For complexes **7c-f** and **8c-f**, ΔG° was found to be negative for all solvent ratios where switching was observed. For some of the complexes (**7b,d,e** and **8b,d,e**), the value of ΔG° is the most negative at 90% THF- d_8 , because switching was not observed until around 180 K for the samples in THF- d_8 , possibly the result of a shift in the value of E_T^N at which the preference for one isomer switches because of the less electron donating ligands, which negates the preference for outer sphere Cl^- coordination, thereby resulting in the semi-open isomer and limiting the range of temperatures over which the switching could be observed as well as the magnitude of the changes.



ΔG° and K_{eq} also can be compared between complexes to correlate the electron donating/withdrawing abilities of the ligands to the preference of one isomer over the other. As was mentioned above, for the complex with the most electron withdrawing groups on the ligands, only the semi-open isomer **8g** was observed in all solvent ratios and temperatures investigated. For the complexes with one fluorine on each aryl group, **7f** and **8f**, the value of K_{eq} in THF- d_8 was the largest observed by three orders of magnitude (6.4×10^5) compared to the other four complexes, signifying that at 298 K > 99% of the complex exists as the semi-open isomer (**8f**). While for the other four complexes between 94-99% is present in the semi-open form in THF- d_8 at 298 K. Among the complexes with electron donating methyls on the aryl groups, there is a trend towards smaller K_{eq} values, although the only K_{eq} less than one was for complexes **7b** and **8b**. As was mentioned above, for some of the complexes ΔG° is the most negative, and K_{eq} is the largest, in a solvent mixture of 90% THF- d_8 . If one compares the values of ΔG° at this solvent mixture, it correlates well with the electron donating/withdrawing behavior of the ligands with ΔG° decreasing as the electron donating ability of the ligand decreases, **c** > **b** > **d** > **e** > **f**. The value of ΔG° for complexes **7c** and **8c** is larger than that of complexes **7b** and **8b**, possibly because sterics begin to be a factor that influences the preferred geometry with complexes **7b** and **8b**, as a result of the two ortho methyl groups on the ligand. Interestingly, the shift in equilibrium between the two isomers depends on the solvent ratio (THF- d_8 :CD₂Cl₂) and, in addition, this equilibrium shift can be reversed by changing the solvent mixture back to the original solvent ratio, suggesting that solvent polarity is the most important contributor to the preference of one isomer over the other, with more polar solvents stabilizing the charges between a non-coordinated counterion and a positively charged metal complex, solvating the non-



coordinated counterion and favoring the closed isomer. Less polar solvents cannot solvate outer sphere coordination counterions, resulting in the Cl⁻ moving into the inner coordination sphere, displacing one of the S-Rh bonds, forming the semi-open isomer (**Figure 9**). This new understanding of the factors that influence the coordination geometry of Rh^I(PS)₂Cl complexes allows one to tailor both the solvent and the electron donating/withdrawing ability of the ligands to achieve a targeted functional WLA system.

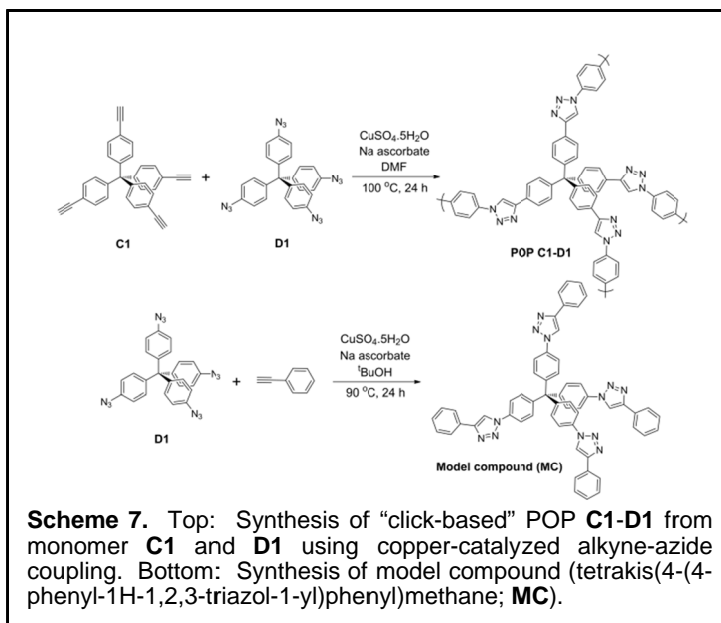
Objectives 2 and 3: MOFs capable of recognizing and separating molecules in novel and efficient ways and structures that facilitate directional energy transfer.

5. A “Click-based” Porous Organic Polymer from Tetrahedral Building Blocks.

Highly crosslinked, microporous organic polymers have recently received significant attention as potential materials for a variety of applications ranging from gas storage and gas separation, to chemical catalysis, chemical sensing, and capture of improvised chemical threats such as ammonia. Depending on the design, synthetic strategy, and properties, these materials have been classified into several sub-sets including amorphous hyper-cross-linked polymers (HCPs), polymers of intrinsic microporosity (PIMs), conjugated microporous polymers (CMPs), porous organic polymers (POPs), porous organic frameworks (POFs), and (crystalline) covalent organic frameworks (COFs). Regardless of the degree of crystallinity, the pore properties of these materials can often be modulated based on the choice of the building blocks. Notably, organic materials with high surface areas can be made from all-planar building blocks as well as from combinations of non-planar “struts”. Herein, we report the synthesis of a highly stable, microporous “click-based” porous organic polymer (POP) *via* copper-catalyzed alkyne-azide coupling (CuAAC) between two rigid tetrahedral building blocks ($T_d + T_d$).

Alkyne-azide “click” chemistry has been widely employed in the syntheses of both linear and cross-linked polymers with diverse applications ranging from drug delivery to electronics. Our groups have applied this strategy in the modification of porous materials such as MOFs and nanobins. Given the aromatic, rigid nature of the 1,2,3-triazole group that results from alkyne-azide coupling, we reasoned that highly cross-linked organic polymers synthesized using this strategy would possess permanent microporosity and be attractive materials for gas storage. In addition, the high stability of the 1,2,3-triazole linkage could give “click-based” POPs thermal and chemical stability advantages over other polymers obtained via alternative bond-construction strategies.

The CuAAC reaction between tetrakis(4-ethynylphenyl)methane (**C1**) and tetrakis(4-azidophenyl)methane (**D1**) (**Scheme 7**) occurs readily in dimethylformamide (DMF) at both room temperature and 100 °C to give several versions of POP **C1-D1** as brown powders. Since the surface area of the POP synthesized at 100 °C ($1260 \text{ m}^2 \text{ g}^{-1}$) was much higher than the version synthesized at 25 °C ($440 \text{ m}^2 \text{ g}^{-1}$), further optimization of the synthesis was carried out at the higher temperature. The yield for POP **C1-D1** (**Table 1**) was almost quantitative, suggesting that crosslinking was nearly complete with no soluble oligomers. However, care must be taken in isolating the product as a fraction in fine particulates can be lost if the filtration is carried out over filter paper (**Table 1**).



Loss of this component during the filtration process can result in a slight decrease of the specific surface area of the overall product ($1360 \text{ m}^2\text{g}^{-1}$ vs. $1440 \text{ m}^2\text{g}^{-1}$, **Table 1**) but does not significantly affect the micropore and total pore volumes.

Because the progress of CuAAC depends on the availability of Cu^{I} intermediates, which in turn depends on the amount of sodium ascorbate reducing agent, we optimized the porosity of the product POP **C1-D1** by adjusting the amount of sodium ascorbate between 10 and 70 mol%, while keeping the amount of copper catalyst constant (10 mol%). Surprisingly, the surface area of POP **C1-D1** systematically decreased with increasing amount of sodium ascorbate in the reaction mixture (**Table 1**). Treatment of the POP via Soxhlet extraction (to remove any sodium ascorbate possibly present in the pores), did not result in improvement in the original surface area. It is possible that at higher loadings of ascorbate more Cu^{I} can be available, allowing for more crosslinking to occur within the porous network and thus lower surface areas.

This hypothesis is supported by a progressive decrease in micropore volumes and total pore volumes as the amount of ascorbate is increased.

The FTIR spectrum of POP **C1-D1** (**Table 1**) compares well with that of a model compound (**MC**, **Scheme 7**). A broad $\text{N}=\text{N}$ stretch can be observed at 1610 cm^{-1} (**Figure 10**), together with a weak $\text{C}=\text{CH}$ band at 3029 cm^{-1} , consistent with the formation of the expected triazole ring. However, IR stretches from unreacted azide could still be observed at 2114 cm^{-1} , suggesting that the azide-alkyne coupling is incomplete. Interestingly, a strong and broad stretch at $\sim 3300 \text{ cm}^{-1}$ is also observed, suggesting the presence of significant amounts of physisorbed water. The solid state ^{13}C CPMAS NMR spectrum of POP **C1-D1** (**Figure 11**) matches well with that of **MC**, further supporting the formation of cyclic triazole linkages.

Table 1. Surface-area and pore properties of “click” POP **C1-D1** synthesized by varying the amount of sodium ascorbate.

*Entry	sodium ascorbate (mol %)	Specific surface area (m^2g^{-1}) ¹⁾	Micropore volume (cm^3g^{-1})	Total pore volume (cm^3g^{-1})	Yield (%)
1a ^a	10	1440	0.56	0.76	>99
1b ^b	10	1360	0.53	0.74	67
2 ^b	20	1320	0.51	0.73	62
3 ^b	30	1260	0.49	0.67	64
4 ^b	50	1140	0.44	0.64	81
5 ^b	70	1090	0.42	0.52	77

*All reactions were carried out in DMF at 100°C using 10 mol% $\text{CuSO}_4 \cdot 5\text{H}_2\text{O}$ and at 0.04 M acetylene functional group concentration. ¹⁾Obtained using workup procedure II. ²⁾Obtained using workup procedure I.

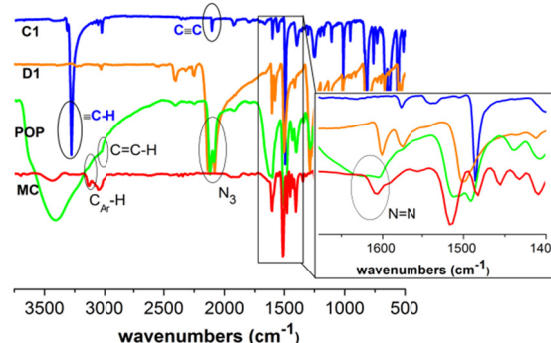


Figure 10. FTIR spectra of the starting materials (**C1** and **D1**) and POP **C1-D1** (**Table 1**, entry 1b).

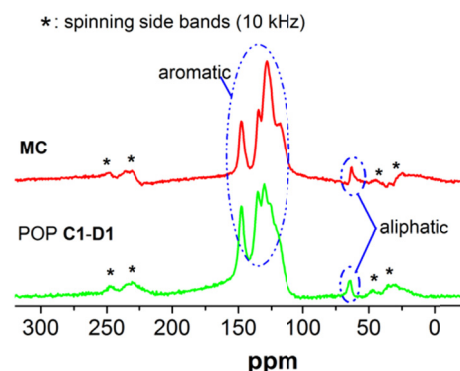


Figure 11. ^{13}C CPMAS NMR spectra of the model compound (**MC**) and POP **C1-D1** (**Table 1**, entry 1b).

Thermogravimetric analysis (TGA) of dried POP **C1-D1** shows that this microporous material is thermally stable, losing only 20 wt% of its mass below 500 °C. The polymer's powder X-ray diffraction spectrum is featureless, implying (as expected) that it is amorphous.

Consistent with the anticipated chemical stability of the 1,2,3-triazole linkage, POP **C1-D1** is remarkably stable approaching the stability of the most stable metal organic framework analogues. Immersing **C1-D1** in 6 N NaOH (aq) or 6 N HCl (aq) at 60 °C for 8 h leads to essentially no change in internal surface area. Increasing the immersion temperature to 80 °C and time to 24 h, leads to only slight decreases (10-12%) in surface area. The stability of the cyclic-triazole-linked polymer greatly exceeds that of imine-linked POPs having comparable initial surface areas; the surface areas of the latter rapidly decrease following exposure to water. **C1-D1** also displays stability superior to those of dimide-linked POPs, which are stable in relatively dilute aqueous acids (0.1 N) but not in bases.

High uptake of nitrogen at low pressure, as observed in the N₂ adsorption-desorption isotherms for the various preparations of POP **C1-D1** (**Figure 12**), suggests that these materials are mainly microporous. However, the isotherms of POPs prepared with smaller amounts of sodium ascorbate (10-30 mol %) tend to exhibit more hysteresis than those prepared with larger amounts (50-70 mol %). The slopes of the isotherm adsorption branch for the latter materials are also less steep than those for the former. Particularly interesting is the presence of a pronounced hysteretic step in the N₂ isotherm desorption branch for the POPs prepared with low amounts (10-30 mol %, **Table 1**, entries 1a-3) of sodium ascorbate (**Figure 10**). In contrast, there is no hysteretic step in the N₂ isotherm desorption branch for the POPs prepared by using higher amounts (50-70 mol %, **Table 1**, entries 4 and 5) of sodium ascorbate (**Figure 10**).

For the samples whose isotherms contain no hysteretic desorption step (**Figure 14** and **Table 1**, entry 5), the parallel, almost-horizontal nature of the two branches of the isotherm implies the presence of only narrow slit-like pores. In contrast, the samples whose isotherms contain a hysteretic desorption step (**Figure 12** and **Table 1**, entry 1b) likely possess more complex pore geometry. The near-horizontal desorption behavior in the $0.5 < P/P_o < 1$ region and the abrupt switch into a slightly steeper desorption behavior in the $P/P_o < 0.5$ region (for N₂ adsorption at 77 K, this switch often occurs near the $P/P_o = 0.42$ point) indicates that the pores are not all slit-like. The upward-sloping trend in the adsorption branch of these isotherms, which becomes steeper at higher pressures, has been attributed by others to the presence of pores of different shapes and sizes (mainly microporous with some higher micropores and lower mesopores).

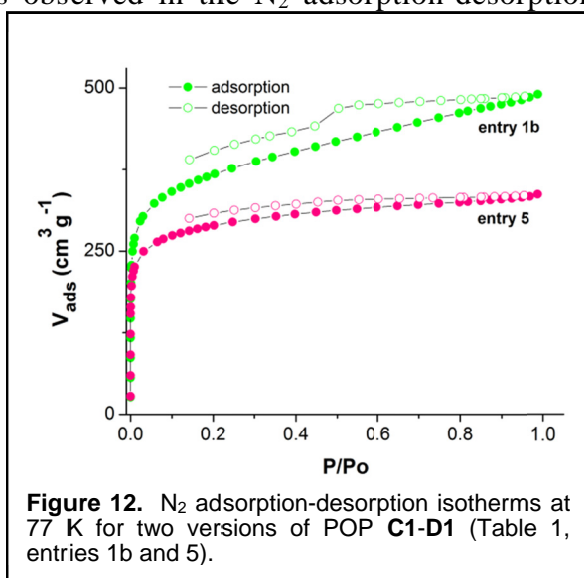


Figure 12. N₂ adsorption-desorption isotherms at 77 K for two versions of POP **C1-D1** (**Table 1**, entries 1b and 5).

Despite the aforementioned indications of complex pore geometry, non-local density functional theory (NLDFT) pore size distribution analysis of POP **C1-D1** prepared using 10 mol% sodium ascorbate (**Table 1**, entry 1b) indicates a mainly microporous material with a narrow pore-size distribution centered around a primary pore width of 9.2 Å (**Figure 13**). This width is much smaller than expected (~21 Å) for an idealized diamond-like single network formed by simply clicking together monomers **C1** and **D1**. The disparity constitutes strong evidence for interpenetration of the hyper-crosslinked networks constituting POP **C1-D1**.

Given the high surface area and narrow pore-

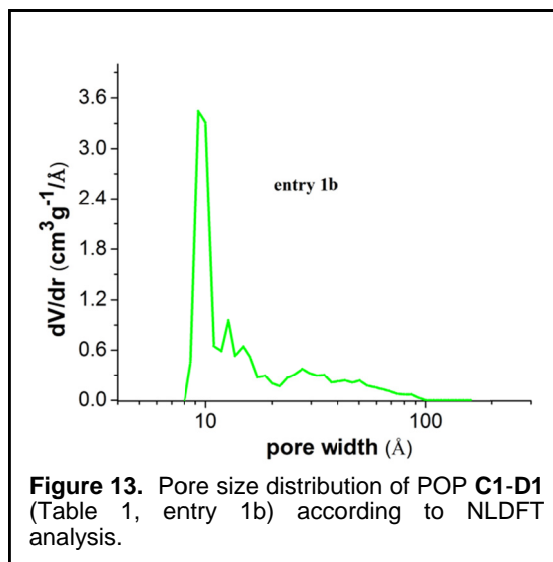


Figure 13. Pore size distribution of POP **C1-D1** (**Table 1**, entry 1b) according to NLDFT analysis.

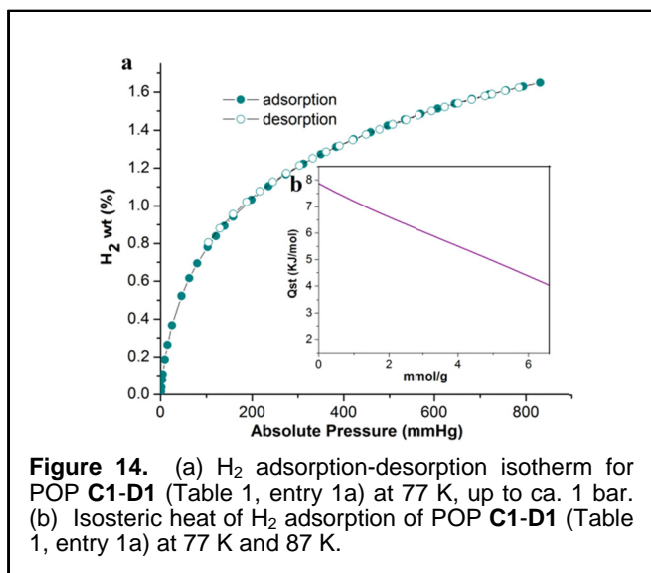


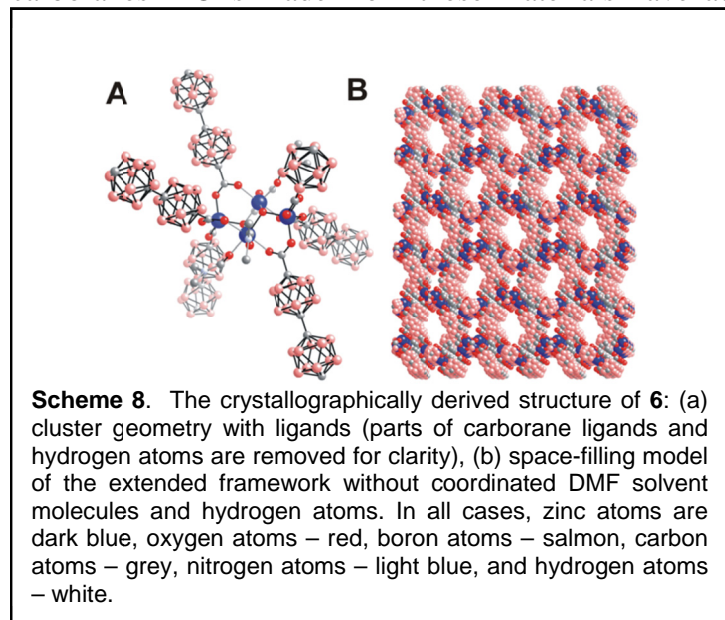
Figure 14. (a) H₂ adsorption-desorption isotherm for POP **C1-D1** (**Table 1**, entry 1a) at 77 K, up to ca. 1 bar. (b) Isothermic heat of H₂ adsorption of POP **C1-D1** (**Table 1**, entry 1a) at 77 K and 87 K.

kJ mol⁻¹ at 1 bar (**Figure 14b**). These values are typical for H₂ adsorption in micropores of materials that can offer only London dispersion type interactions.

In summary, we have shown that a permanently microporous POP can be assembled readily from a complementary pair of tetrahedral building blocks (T_d + T_d) using CuAAC chemistry. The resulting material is thermally stable, as well as chemically stable – easily surviving exposure to highly acidic and basic solutions. At least at 1 bar, the material's micropores provide for reasonably good ambient-temperature adsorption of CO₂ and cryogenic adsorption of H₂. The excellent stability of POP **C1-D1** suggests more generally that cyclic-triazole-linked POP materials can serve as excellent engineering materials under a wide range of conditions. We are actively exploring structure-property-relationships for these types of materials and efforts to turn them into high surface-area and morphologically well-defined nano- and microparticle structures, similar to infinite coordination polymer particle analogues. Such capabilities will allow researchers to tune the properties of this novel class of materials for optimal performance in many practical applications, including gas storage, catalysis, and biological probe design.

6. Second Generation of Carborane-Based Metal Organic Framework (MOFs) Materials.

Recently, we developed a series of robust microporous materials based upon icosahedral carboranes MOFs made from these materials have advantages compared to many aryl-based

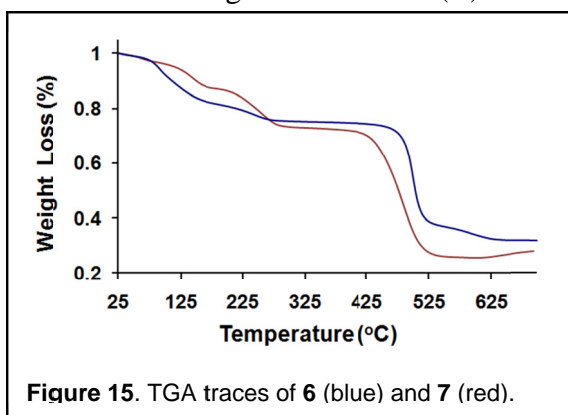


systems with regard to structural rigidity and thermal and chemical stability. Prior studies have utilized dicarboxylated *p*-carboranyl ligands and Zn(II) and Co(II) salts to create MOFs and, more generally, infinite coordination polymer (ICP) materials. In general, these materials exhibit unprecedented stability with respect to thermal degradation, allowing them to undergo activation by heating under vacuum. Such activation leads to uncoordinated metal sites in the pores, which significantly enhance hydrogen gas uptake and influence selectivity in gas mixture separation experiments. Herein, we report the synthesis of two

ligands based on *p*-carborane and the MOF structures prepared from them. These MOFs exhibit significantly higher surface areas than their single carborane predecessors.

We have selectively functionalized *p*-carborane to form the rigid, linear ligand precursors via Cu(I) coupling chemistry. The chemical orthogonality of the BH and CH moieties in the carborane unit permits one to selectively derivatize it, which cannot be easily accomplished with polyaryl analogs. Solvothermal reactions of extended carborane-based ligands with Zn(II) nitrate salt in appropriate solvent mixtures yield crystalline MOFs **6** and **7**, respectively. Both materials were characterized in the solid-state by single crystal X-ray diffraction analyses (*vide infra*). MOF **6** was prepared by a solvothermal reaction between Zn(II) nitrate hexahydrate and ligand **3** in a 1:1:1 mixture of dimethylformamide (DMF), diethylformamide (DEF), and ethanol (EtOH). A single crystal X-ray diffraction study of **6** revealed that it crystallizes in the monoclinic space group, $P2_1/c$. It is a 3D open framework with repeating secondary building units (SBU) comprised of $Zn_4(OH)_2(DMF)_4$ metal clusters (**Figure 15**); ligand **3** serves as a connector between the Zn-based nodes, which binds in two distinct modes, η^1 and η^2 (**Figure 1A**).

MOF **7** was prepared by a solvothermal reaction between ligand **5** and Zn(II) nitrate hexahydrate in a 1:1:1:1 mixture of DMF, DEF, EtOH, and water. Single crystal X-ray analysis revealed that **7**, unlike **6**, is a 2D framework composed of 1D layers stacked in an ABAB arrangement, with a triclinic P_1 space group (**Figure 16**). The framework for **7** consists of dinuclear $Zn_2(H_2O)(EtOH)$ SBU clusters interconnected in a paddle wheel fashion, with four dianionic ligands **5** (η^2 fashion) to form a 2D infinite layer (**Figure 16A**). The phase purity of **6** and **7** prepared in bulk was confirmed by



comparing the powder diffraction pattern (PXRD) of the samples with the patterns generated from single-crystal diffraction data. As suggested by TGA analysis, both **6** and **7** can be activated in a manner that retains their crystallinity. Within **6**, clathrated solvent molecules exit the framework between 100-170 °C, followed by coordinated DMF molecules in the 240-290 °C temperature range (Figure 15). Decomposition of **6** is observed only at 510 °C, which is significantly higher than most Zn(II) aryl-based MOFs (350-400 °C). A sample of **6** was thermally activated at 250 °C for 20 h under dynamic vacuum (0.01 mTorr), providing activated material **6'**. This procedure results in complete solvent loss (both clathrated and coordinated at SBUs), as evidenced by CP-MAS ^{13}C NMR spectroscopy. Indeed, resonances at δ 25 corresponding to DMF molecules are not observed in **6'**, in contrast with the parent material **6**. Resonances corresponding to ^{13}C -atoms in ligand **5** (δ 165 and 75) in **6** and **6'** do not change during activation, suggesting that the framework remains chemically intact. Volumetric gas sorption measurements of **6'** using N_2 were used to verify its microporosity. Indeed, it exhibits a reversible Type 1 isotherm (Figure 17A). Importantly, the calculated surface area (Brunauer, Emmett, Teller - BET = 1180 m^2/g) is the largest for any studied carborane-based MOF thus far, which is a direct consequence of the extended ligand design approach explored in this work.

Similar to **6**, the TGA data indicate that **7** undergoes solvent-loss mass changes over the 100-160 °C (clathrated molecules) and 180-270 °C (coordinated solvent molecules-water/ethanol) temperature ranges (Figure 15). The resulting porous framework begins to decompose only above 425 °C. PXRD studies reveal that **7** retains its crystallinity even after solvent molecules have been removed completely. Thermal treatment of **7** under vacuum (200 °C, 15 h, 0.01 mTorr) leads to **7'**, which has a microporosity of 800 m^2/g as determined by CO_2 volumetric gas sorption and NLDFT (nonlocal density functional theory) modeling (Figure 17B). The stability of material **7** is likely due to its unique stacking structure, which prevents the loss of porosity even when solvent molecules are removed and the layers shift closer to each other.

These materials are robust and can be activated thermally, resulting in highly porous structures. Indeed, to date these are the most porous carborane-based MOFs realized, and their properties point to potential use in gas separations.

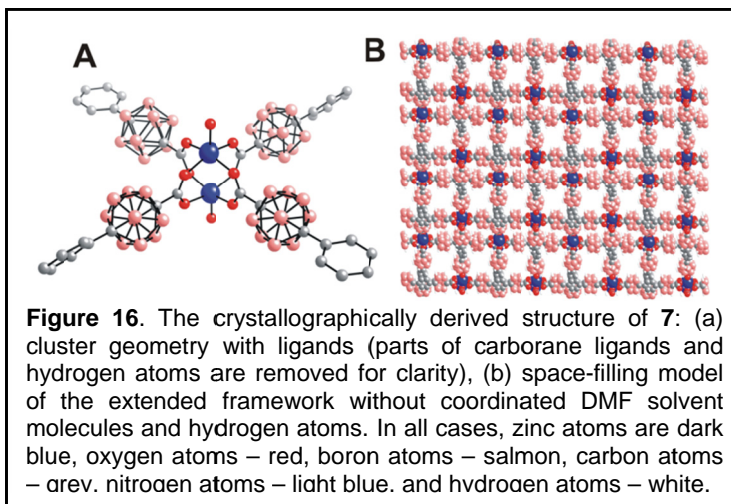


Figure 16. The crystallographically derived structure of **7**: (a) cluster geometry with ligands (parts of carborane ligands and hydrogen atoms are removed for clarity), (b) space-filling model of the extended framework without coordinated DMF solvent molecules and hydrogen atoms. In all cases, zinc atoms are dark blue, oxygen atoms – red, boron atoms – salmon, carbon atoms – grey, nitrogen atoms – light blue, and hydrogen atoms – white.

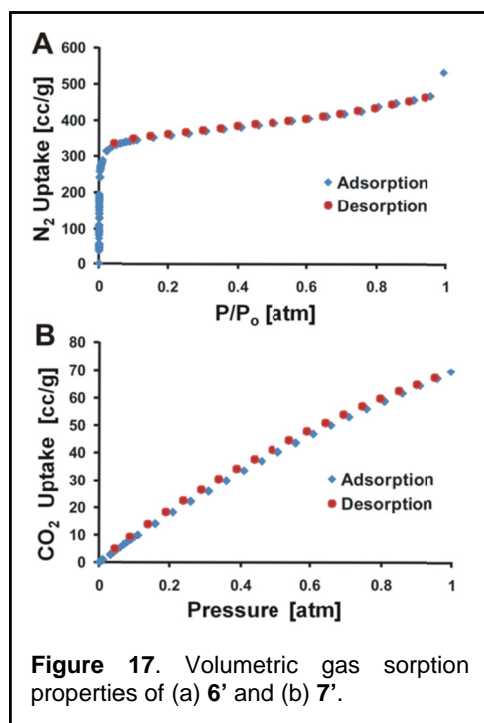


Figure 17. Volumetric gas sorption properties of (a) **6'** and (b) **7'**.

7. Nickel (III)/(IV) Bis(dicarbollide) as Redox Shuttle in Dye-Sensitized Solar Cells.

Dye-sensitized solar cells (DSCs) have displayed significant potential to compete with silicon-based cells in the future. Traditional DSCs rely on a high-surface area, nanoparticulate TiO_2 framework, chemisorbed with a monolayer of high molar extinction dye to harvest the majority of incoming photons. O'Regan and Grätzel originally developed DSCs utilizing an iodine-based liquid electrolyte (I^-/I_3^-), which efficiently regenerates a ruthenium-based polypyridyl dye and employs a platinized counterelectrode which facilitates the reduction of I_3^- to I^- . With simply a handful of alternative redox shuttles studied to date, only a select few exhibit competitive DSC characteristics to that of I^-/I_3^- . However, as I^-/I_3^- DSCs have reached a local maximum, new alternative redox shuttles need to be developed in order to realize higher efficient DSCs.

Recently, we reported a new metallocarborane-based redox shuttle utilized in DSCs, exhibiting power conversion efficiencies far superior than that of the previously studied ferrocene/ferrocenium redox couple. Structurally similar to metallocenes, the Ni(III/IV) bis(dicarbollide) metallocarborane consists of two η^5 coordinated dicarbollide ligands ($\text{C}_2\text{B}_9\text{H}_{11}^{2-}$), sandwiching the metal center. Moreover, depending on whether the metal is in the Ni(III) or Ni(IV) state, the equatorial carbons can be positioned either in a trans or cis conformation. This chemically inert and thermally robust Ni(III)/(IV) bis(dicarbollide) shuttle not only has longer electron lifetimes than ferrocene/ferrocenium, but also advantageously exhibits fast dye regeneration. Additionally, the dicarbollide moiety can be easily derivatized to tune the electrochemical potential of the redox couple, making such system an attractive class of noncorrosive shuttles. Yet, due to the fast charge interception dynamics by the Ni(IV) bis(dicarbollide) specie, more work is necessary to improve the current densities from these cells in order to be competitive with I^-/I_3^- .

Here we present aerogels as a preferable framework over nanoparticles for DSCs utilizing the Ni(III/IV) bis(dicarbollide) redox shuttle. Alternative semiconducting frameworks have been extensively studied for DSCs in hopes to improve the optical absorptivity and electron transport properties in the devices. Structures include hollow microspheres and nanotubes, and more recently, surface modified- SiO_2 aerogels have also shown to be feasible templates for charge collection. In the past, aerogels have attracted attention due to their impressive strength-to-weight ratios. As their synthesis involves a simple sol-gel process, aerogel production can be readily scaled-up. More importantly, aerogel porosities and film thicknesses can be effectively controlled, with pore sizes from a few nanometers to the micron range, and film thicknesses controlled down to 1 micron. Thereby, upon facile deposition of a semiconductor via atomic layer deposition (ALD) on the SiO_2 framework, the resulting rigid aerogel

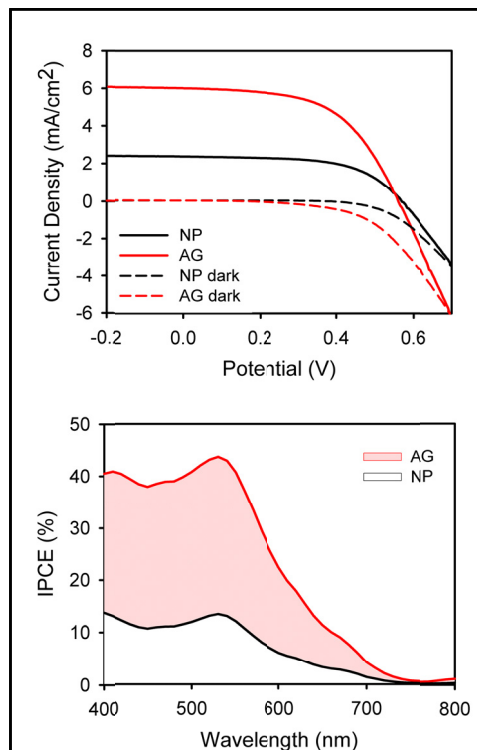


Figure 18. Comparison of Ni (III)/(IV) bis(dicarbollide) DSCs fabricated with 8 μm thick SiO_2 aerogel film coated with 10.5 nm of TiO_2 and nanoparticulate film consisting of ~ 25 nm diameter TiO_2 particles: a) J - V characteristics and (top) b) incident photon-to-current conversion efficiencies (bottom).

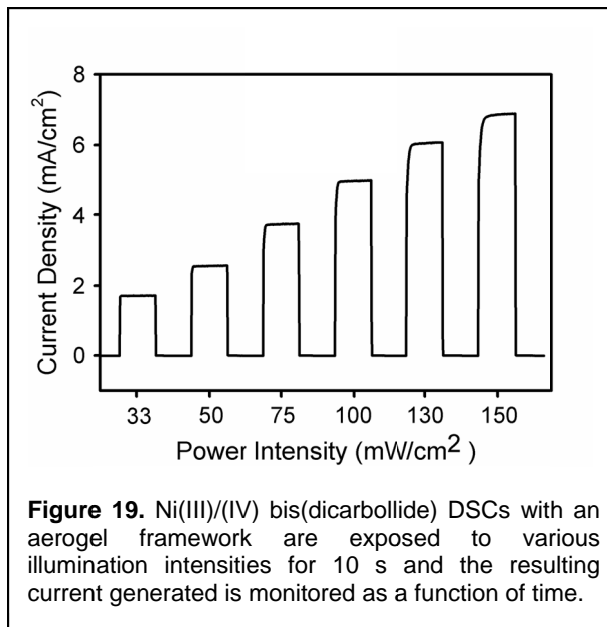
films can be used as DSC photoanodes. Through ALD, a large variety of metal oxides (i.e. ZnO, NiO, SnO₂) can be conformally coated on the rough aerogel surface, making this porous structure applicable to many types of solar cells.

Utilizing the aforementioned SiO₂ aerogel framework, we observe enhancements in short-circuit current densities (J_{sc}) from 2 mA/cm² in nanoparticles to over 6 mA/cm² in aerogels (**Figure 18**). As a result, DSC performances are significantly improved, achieving power conversion efficiencies of over 2% for this Ni(III)/(IV) shuttle, as compared to 0.8% with a TiO₂ nanoparticulate photoanode. This improvement is also reflected in the incident-to-current conversion efficiencies (**Figure 18B**), where significantly more photons are harvested at the N719 absorption maximum at 535 nm.

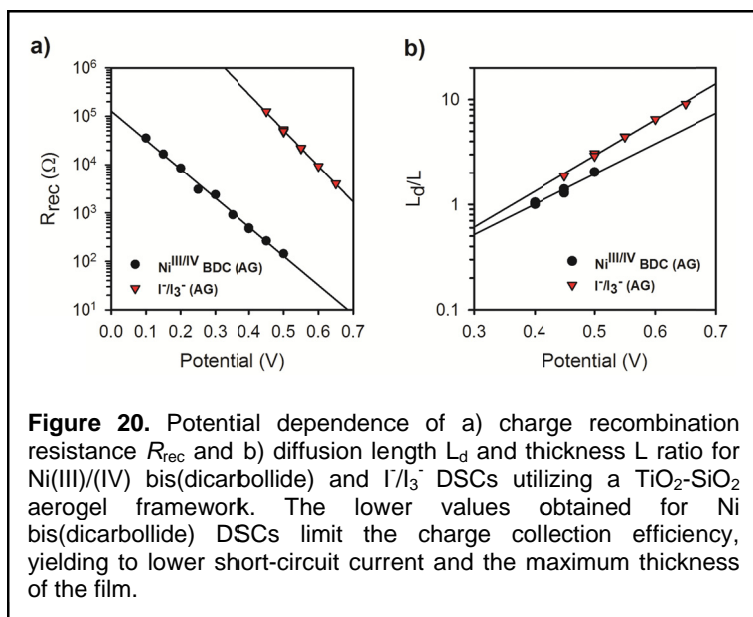
Unlike cobalt-based redox shuttles, the Ni(IV) bis(dicarbollide) does not suffer from significant mass-transport issues of the oxidized shuttle species. Therefore, there is a linear correlation between illumination intensity and J_{sc} generated up to 1 sun illumination for devices incorporating the TiO₂ nanoparticle and aerogel frameworks. However, from the current transients (**Figure 19**), where the aerogel DSC behavior under light intensities up to 1.5 suns (150 mW/cm²) is monitored in 10 s intervals, the current generated at light intensities above 1 sun does not immediately achieve its J_{sc} value. Since a low concentration of Ni(IV) is utilized in the electrolyte to minimize electron interception, the diffusion of the oxidized form to the counterelectrode to regenerate itself could be limiting current generation, giving rise to the slope observed before the cell can achieve its steady-state current. However, this does not appear to adversely affect overall device performances past 1 sun illumination, with power conversion efficiencies ~ 3% (i.e. V_{oc} = 660 mV, J_{sc} = 6.7 mA/cm², FF = 60%, η = 2.8%) for a DSC utilizing a 8.0 μ m thick aerogel photoanode) under 150 mW/cm².

Thus, the porous aerogel structure ensures good penetration and diffusion of electrolytes such as the prolate spheroid shaped Ni-based metallacarborane shuttle and could potentially alleviate mass-transport issues with bulkier DSC redox shuttles.

To investigate the various kinetic process occurring across the multiple interfaces in the TiO₂ nanoparticle and aerogel-based DSCs, electrochemical impedance spectroscopy (EIS) is utilized. With the proper model, steady-state DSC characteristics such as electron transport resistance through the TiO₂ network R_t , charge transfer resistance at the TiO₂/electrolyte R_{ct} , and the TiO₂ chemical capacitance C_{μ} , can be extracted from the frequency dependent response to a modulate small perturbation in the external electrical potential as a function of the applied bias voltage. Bisquert, et al. have developed a physically relevant transmission line model for DSCs utilizing the I/I₃⁺ redox shuttle to derive these constant elements. Therefore, electron diffusion coefficient $D_n = (R_t C_{\mu})^{-1}$, lifetime $\tau_n = R_{ct} C_{\mu}$, and effective diffusion length $L_n = L(R_{ct}/R_t)^{1/2} = (D_n \tau_n)^{1/2}$ can be calculated to evaluate DSC performance. Applying the same transmission line model to DSCs utilizing the Ni(III)/(IV) bis(dicarbollide) redox shuttle, recombination resistances at the



TiO₂/electrolyte interface were determined to be $\sim 10^2$ smaller for the Ni bis(dicarbollide) system (**Figure 20**). Comparable results were obtained from the open-circuit voltage (V_{oc}) decay technique, where electron interception rates by Ni(IV) bis(dicarbollide) from the TiO₂ photoanode were 10^2 times faster than that by I_3^- , contributing to the lower V_{oc} 's expected as compared to the I^-/I_3^- system.⁴ Consequently, diffusion lengths are noticeably lower for the metallacarborane system as seen in Figure 6b, where the ratio of the effective diffusion length L_d to photoanode thickness L is plotted against applied potential. Here, the impedance experiments are performed in the dark with DSCs utilizing a 10 μ m thick TiO₂-coated SiO₂ aerogel photoanode, with the resulting L_d/L obtained for the Ni(III)/(IV) bis(dicarbollide) approximately half of I^-/I_3^- around their open-circuit voltage potentials (**Figure 20B**).



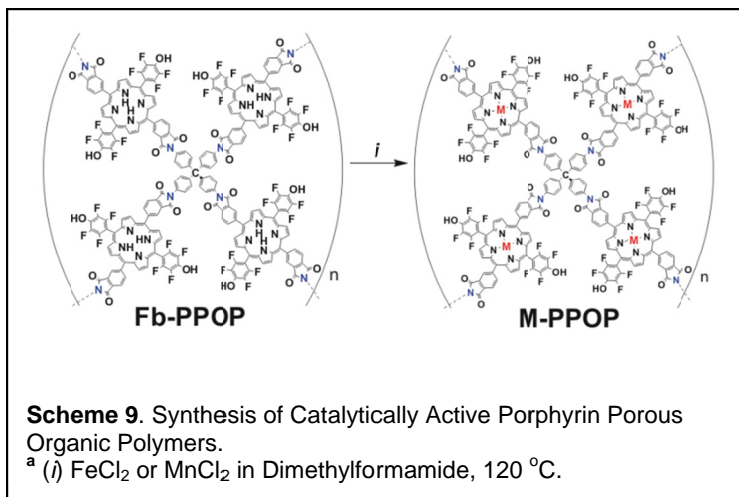
8. Synthesis, Properties and Gas Separation Studies of Catalytically Active Robust Diimide-based Microporous Organic Polymers.

Microporous materials have attracted considerable recent attention because of a wide variety of potential applications, including catalysis, gas storage, and chemical separations, among many others. In addition to traditional materials such as zeolites, a number of newer classes of microporous materials have been described, including metal-organic frameworks (MOFs), covalent-organic frameworks (COFs), polymers of intrinsic microporosity (PIMs), porous organic polymers (POPs), and others. MOFs have been the most widely studied of these newer materials—partly because of their well-defined crystalline structure and partly because of the available enormous variety of candidate organic struts. A great deal of attention has been given to catalytic applications in MOFs, due to the potential for integrating the well-defined, single-site activity of homogenous catalysts with the shape-, size-, chemo-, and enantio-selectivity that can be designed into the micropores. However, incorporation of catalytic struts with active metal sites has proven to be a significant challenge due to the difficulty in preventing an erstwhile catalytic center from acting as a structural node. To avoid this complication, the synthesis of all-organic materials, where all the nodes are formed via organic reactions, is an attractive alternative strategy for incorporating catalytically active complexes into porous frameworks.

Metalloporphyrins are particularly desirable to use as struts in porous materials given their well-studied catalytic behavior. Specifically, Fe and Mn(porphyrins) are analogues of the heme cofactor in the biologically ubiquitous family of cytochrome P450 enzymes, which are responsible for catalyzing a wide variety of oxidation reactions. However, several factors limit the application of these synthetic heme analogues as oxidation catalysts. Most importantly, synthetic metalloporphyrins can rapidly become deactivated, either through the oxidative degradation of the porphyrin ring, or formation of μ -oxo dimers. Nature avoids

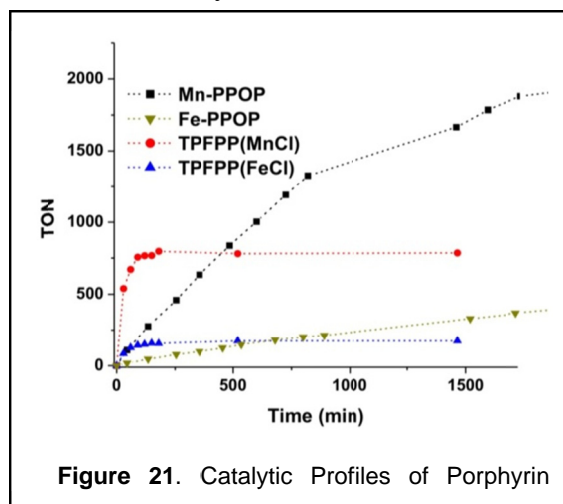
these problems by enveloping the heme moiety within a large protein structure, which can also engender selectivity by controlling substrate access to the active site. By incorporating metalloporphyrins within microporous materials, it is hoped that these essential features of biological systems can be mimicked.

This challenge motivated us to apply our recently reported modular strategy for synthesizing diimide-linked porous organic polymers (POPs) to the problem of constructing POPs containing free-base porphyrin subunits. The resulting highly rigid, all-organic porous materials should be amenable to post-synthesis modification (PSM) to yield a wide range of metalloporphyrin-based polymers for chemical catalysis. The synthesis of POPs previously developed by our group and others takes advantage of the condensation reaction between amines and acid anhydrides to form robust diimide bonds. Porphyrins can be incorporated into POP structures by utilizing free-base porphyrins with either pendant amine or acid anhydride groups (**Scheme 9**). To introduce 3-dimensional pores into the POP network, we employed the easily accessible tetraamine monomer **1** and a bifunctional porphyrin monomer with acid anhydride groups. Condensation of the free-base porphyrin monomer with **1** proceeded readily in refluxing propionic acid to give a porous material (surface area $\sim 400 \text{ m}^2/\text{g}$). This free-base porphyrin POP (**Fb-PPOP**) could be readily metallated with FeCl_2 or $\text{MnCl}_2 \cdot 4\text{H}_2\text{O}$ to give either **Fe** or **Mn-PPOP**. The M-PPOPs both showed highly similar porosity as the **Fb-PPOP**, based on both thermogravimetric analysis and CO_2 uptake.



In the presence of a variety of terminal oxidants, Fe and Mn(porphyrin) complexes are well-known to function as catalysts for a range of oxidation reactions. To test the catalytic activity of the metallated PPOPs (M-PPOPs), we examined the epoxidation of styrene by a soluble analogue of iodosylbenzene (2-(*tert*-butylsulfonyl)iodosylbenzene). (This oxidant is known to be unreactive with olefins in the absence of a catalyst.) As a control, these epoxidations were compared against reactions catalyzed by the corresponding metallated *meso*-tetrapentafluorophenylporphyrin homogenous complexes ((TPFPP)M, M = FeCl, MnCl). At 0.025 mol% catalyst loading, the homogenous catalysts rapidly produce epoxides, but with facile deactivation and degradation of the catalyst (after 780 turnovers in the case of (TPFPP)Mn, and 170 in the case of (TPFPP)Fe).

In contrast, both the **Fe**- and **Mn-PPOP** show greater stability than the analogous homogenous catalysts: **Mn-PPOP** is active for more than 2000 turnovers without displaying any signs of

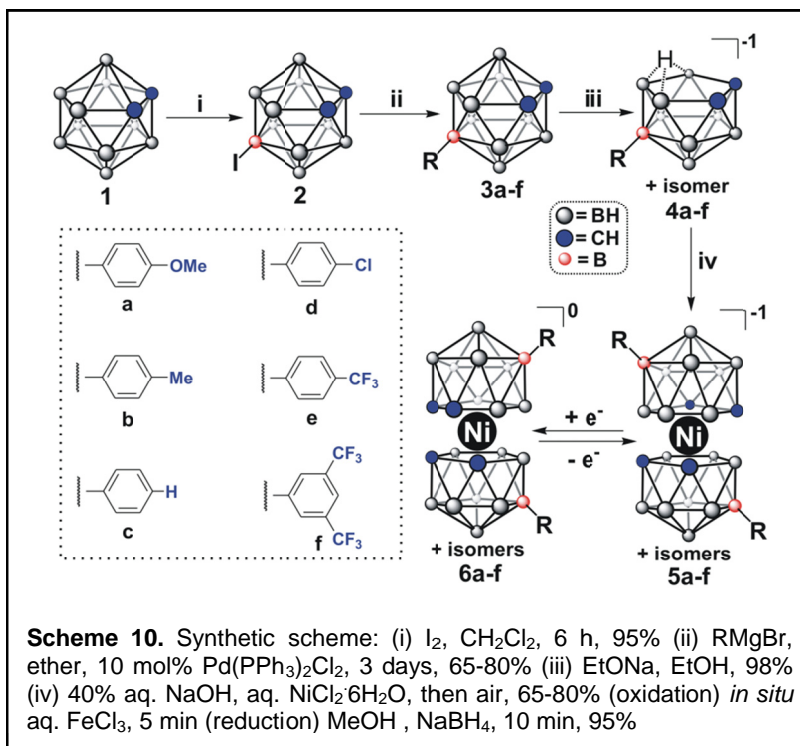


decomposition (**Figure 21**). As would be expected for heterogenous catalysts, M-PPOPs generally display a much slower initial rate than the homogeneous analogs. The new PPOPs also proved catalytic for alkane oxidation, albeit with much lower activity than for expoxidation, as expected for iodosylbenzene oxidant. The oxidation of cyclohexane with 1 mol% of **Fe-** and **Mn-PPOP** produced 12% and 48% yields of product (based on oxidant), respectively. In both cases, the product was a mixture of cyclohexanol and cyclohexanone (97:3 in the case of Fe; 95:5 for Mn).

9. Nickel (III)/(IV) Bis(dicarbollide) as Redox Shuttle in Dye-Sensitized Solar Cells.

Despite identifying shuttles with redox potentials comparable to the anionic I/I_3^- redox couple, researchers have not been able to identify ones with the capabilities of the I/I_3^- system. However, the strong corrosive nature of I/I_3^- is a fundamental limitation on the expansion of DSC architectures and restricts the choice of dye and electrode materials. Based on our previously reported work of using the bis(dicarbollide) Ni(III)/(IV) specie as a redox shuttle we have synthesized a new class of non-corrosive B9- (B12)-modified Ni(III)/Ni(IV) bis(dicarbollide) complexes derived from the systematic functionalization of Ni(III)/Ni(IV) bis(dicarbollide) with electron donating and withdrawing groups. Since the parent Ni(III)/Ni(IV) bis(dicarbollide) has previously exhibited promise as a fast shuttle we sought to see how modification of the cage effects the electronic properties of dye-sensitized solar cells. With this new class of complexes, redox potential can be controlled over a 200 mV range, which overlaps the I/I_3^- redox couple allowing each of these complexes to be studied in the context of DSCs.

Following known literature methods, one can iodinate the B(9) position of *o*-carborane **1** in a 95% yield to form 9-I-carborane **2**, which can be subsequently coupled with aryl-based substituents (**Scheme 10**). For example, stirring RMgBr in the presence of a palladium catalyst (10 mol% $Pd(PPh_3)_2Cl_2$) with **2** yields the aryl substituted carborane derivatives (**3a-f**). Compounds **3a-f** undergo deboronation in ethanolic solution overnight, quantitatively yielding nido-carborane derivatives, isolated as $N[Me_3H]^+$ salts (**4a-f**). Finally, further reaction of complexes **4a-f** in concentrated NaOH solution (40%) in the presence of aqueous excess $NiCl_2 \cdot 6H_2O$ resulted in formation of transient Ni(II) bis(dicarbollide) complexes, which immediately oxidize upon exposure to air and form the Ni(III) complexes (**5a-f**). These compounds are purified by oxidizing them further to their Ni(IV) forms using aqueous $FeCl_3$ and passing the resulting mixture through a plug of silica gel, which affords pure **6a-f**.

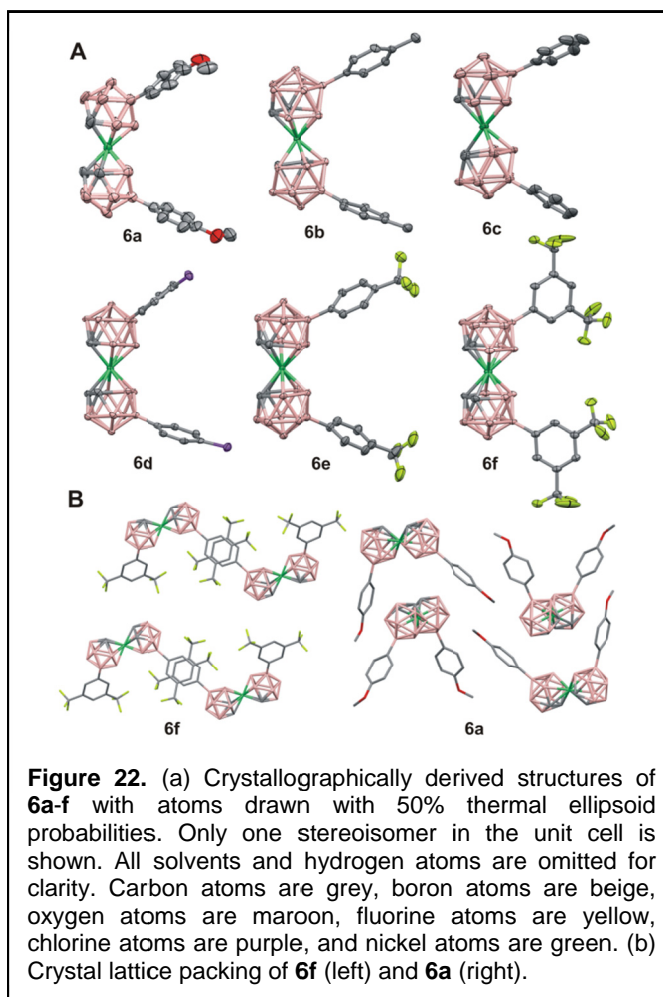


These Ni(IV) compounds can be reduced back to Ni(III) quantitatively with sodium borohydride (NaBH₄) in methanol within minutes, and isolated as tetrabutylammonium (TBA⁺) salts.

In the case of complexes **6a**, **6b**, and **6e** (each dicarbollide cage within the complex is functionalized on the B(9) atom), the meso species were crystallized, whereas in the case of **6c**, **6d**, and **6f**, dd(II) stereoisomers were obtained (dicarbollide cages were functionalized on two isomeric boron positions – 9 and 12). In all cases, one observes a cisoid geometry of the two dicarbollide cages with dicarbollide carbons arranged in a staggered conformation. The carbon-carbon bond distances in **6a-f** show little variation (on average $1.63 \pm 0.03 \text{ \AA}$), regardless of the substituents. This is in contrast with structures with substituents directly on the equatorial C atoms, which exhibit relatively large variation in C-C distances. Although these molecules appear structurally similar, they are all different in color, suggesting significant electronic differences. In particular, we observe a unique crystal packing arrangement for **6f**, where the Ni(IV) center is not interacting with the phenyl moieties (**Figure 22**). This observation may be due to the redistribution of electron density within the molecule induced by the highly polarizing CF₃ functional groups. Compound **6a** is dark blue while **6b** and **6c** are dark red. Compounds **6d** and **6e** are dark orange, and **6f** is light orange, similar to the unfunctionalized Ni(IV) bis(dicarbollide).

DFT calculations on the optimized structures of **6a** and **6e** suggest that this visible absorbance band arises from the intramolecular electron transfer from the filled orbitals of the electron-rich aryl-based moiety to the unoccupied orbital of the electron poor bis(dicarbollide) cage. In the case of **6a**, this transition is lower in energy than that of **6e**, leading to the observed disparity in the Visible band sensitivity for the **6a-6f** series via modulation of the electron withdrawing/donating properties of the phenyl-based functional group. These results suggest that the aromatic character of the bis(dicarbollide) moiety is conjugated, allowing the redox potentials of the **5/6** pair to be influenced by the aromaticity of the aryl groups.

The electrochemistry of **5a-f** and **6a-f** was studied via cyclic voltammetry, and similar to the unfunctionalized Ni bis(dicarbollide), all derivatives undergo quasi-reversible one-electron processes. The $E_{1/2}$ values were measured for each metallacarborane derivative, and they correlate well with the electron donating or withdrawing nature of the chemical substituents. Plotting these potentials against their Hammett constants provides a linear relationship,



indicating that one can tune the electrochemical potential of these complexes simply through choice of substituents (**Figure 23**). This is the first example demonstrating electronic tunability on this kind of Ni bis(dicarbollide) molecules. More importantly, this control allows us to directly probe the effect of varying the redox potential of the Ni bis(dicarbollide) redox couple in a DSC.

A major advantage of this system is the ability to tune the photovoltage of the DSCs through derivatization of the carborane moiety as discussed previously. As the potential difference between the TiO₂ *quasi*-Fermi level and the redox potential is increased, the V_{oc} necessarily must increase. However, complex interplay of various DSC kinetics such as dye regeneration, electron recombination, electron-transfer at the counterelectrode, and shuttle transport through the electrolyte and framework make predicting overall photovoltaic performances a complicated process.¹⁵ Nevertheless, Marcus normal-region behavior is observed with the electron-withdrawing derivatives, where there is an enhancement in V_{oc} in going to more positive shuttle potentials; where the concentration of **6** is held constant to minimize the varying effects of electron capture from the TiO₂ conduction band (i.e. electron interception). However, with the electron-donating derivatives, the V_{oc} is considerably higher than predicted. In fact, the DSCs with **5b/6b** exhibit extraordinary V_{oc} s of 710 mV and even with TiO₂ photoanode ALD modification, no noticeable improvement in photovoltage is observed. By monitoring the TiO₂ conduction band electrons at 980 nm with nanosecond transient-absorption spectroscopy, we observe that the *fast* ($t_{1/2} < \sim 5 \mu s$) electron interception dynamics look similar for all the derivatives, with no noticeable trends with chemical modification of the aryl Ni bis(dicarbollide) moieties.

In conclusion, we demonstrated for the first time that through chemical functionalization of the Ni bis(dicarbollide) moiety in the B(9/12) positions, one can rationally tune the potential of the Ni(III)/Ni(IV) redox pair and readily synthesize these derivatives on the multigram scale. Limited work has been done to probe the importance of the chemical nature of the redox shuttle and major advances need to be made to optimize the electrolyte-dye interaction. The ultimate power of the Ni(III/IV) bis(dicarbollide) system can be realized from the wide range of possible derivatization routes, which not only can alter the redox potential of such motifs, but can be expected to modulate polarity, solubility, binding properties and other molecular parameters. Thus, by rationally designing and extending the approach demonstrated herein, one can expect to gain new fundamental insights and improvements for DSCs employing bis(dicarbollide) as a functional redox core.

10. Light Harvesting and Energy Transport Using Chromophoric Metal-Organic Frameworks (MOFs).

In this part of the project, the light-harvesting ability of extended supramolecular structures – in particular, porphyrin-containing metal-organic frameworks (MOFs) – has been examined. Ethynyl conjugated porphyrins are exceptional chromophores in the red and blue parts of the visible spectrum. Crystalline metal-organic framework (MOF) architectures allow these

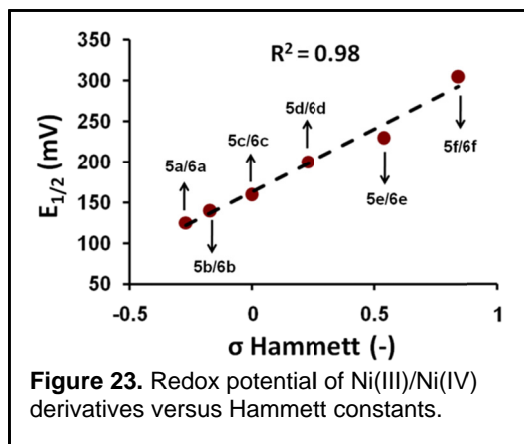


Figure 23. Redox potential of Ni(III)/Ni(IV) derivatives versus Hammett constants.

chromophores to be aligned in optimal fashion for excitonic energy transfer following photon collection.

In order to determine how far excitons can be transferred, we attached electron donors (pyridine-ferrocene) to a small number of the porphyrins and redox-inactive pyridines to the rest. Fluorescence from a photo-excited porphyrin can be quenched by ultrafast electron transfer from the tethered ferrocene. Alternatively, an excited porphyrin lacking a ferrocene tether can transfer its energy to a neighboring porphyrin which, in turn, can transfer the energy to a third porphyrin. The process will continue until either the porphyrin relaxes to the ground electronic state (by emission of a photon), or the exciton reaches a porphyrin that has a tethered ferrocene. By determining the extent to which fluorescence is quenched when only a small fraction of the chromophores have redox tethers (i.e. quenchers) we have determined that, on average, an exciton can visit fourteen chromophores during the brief (ca. 2 ns) lifetime of the photo-excited state (**Figure 24**).

Since each chromophore is ~20 angstroms long, and energy transfer is largely along a single crystallographic axis, we calculate that each exciton can be moved over a nearly 300 angstrom distance. These findings have important implications for coupling light-harvesting arrays to remote catalysts in order to drive useful, endoergic, chemical reactions.

